PAPER • OPEN ACCESS

Gamma-ray spectrometry for burning plasma scenario developments

To cite this article: V.G. Kiptily *et al* 2026 *Nucl. Fusion* **66** 066004

OPEN ACCESS
IOP Publishing | International Atomic Energy Agency
Nuclear Fusion
Nucl. Fusion **66** (2026) 066004 (27pp)
https://doi.org/10.1088/1741-4326/ae5de1

Gamma-ray spectrometry for burning plasma scenario developments

V.G. Kiptily[1,*], Z. Ghani[1], Ye.O. Kazakov[2], on behalf of JET Contributors[a] and the EUROfusion Tokamak Exploitation Team[b]

[1] UKAEA, Culham Campus, Abingdon, Oxfordshire OX14 3DB, United Kingdom of Great Britain and Northern Ireland
[2] LPP-ERM/KMS, Association EUROFUSION-Belgian State, TEC Partner, Brussels, Belgium

E-mail: vasili.kiptily@ukaea.uk

Received 13 November 2025, revised 2 March 2026
Accepted for publication 10 April 2026
Published 7 May 2026

Abstract

Gamma rays generated in nuclear reactions have been used on the Joint European Torus (JET) for more than a quarter of a century to study the main mechanisms of fast-ion slowing down, redistribution as well as for the development of optimal plasma scenarios with auxiliary plasma heating. In future deuterium–tritium (*D–T*) fusion machines, γ-ray measurements, as well as neutron diagnostics, are amongst a very restricted set of plasma diagnostics that will be practical by virtue of their tolerance to the harsh radiation environments they will be required to work within. In this paper, we propose various applications using γ-ray diagnostics during all reactor exploitation phases, from the no-/low-activation to the burning *D–T* plasmas, for the setup of plasma discharges, characterisation of the auxiliary plasma heating, and development of optimal deuterium and *D–T* plasma scenarios. Possibilities of γ-ray diagnostics for α-particle studies in *D–T* and low-activation plasmas are comprehensively discussed. Nuclear reactions generating γ-rays, which are suitable for measurements in fusion devices, have been selected and recommendations for their usage based on their previous experience on JET are given. This paper provides insights for the design and modelling of γ-ray diagnostic systems, as well as testing them in currently working fusion devices before their use in burning plasma machines.

Keywords: fusion plasmas, auxiliary heating, energetic particles, diagnostics, gamma-rays

(Some figures may appear in colour only in the online journal)

1. Introduction

The main source of energy in future thermonuclear reactors with magnetic confinement will be the fusion reaction between deuterium and tritium, $D(T,n)^4He$. The self-sustained *D–T* plasma burn is provided by 3.5 MeV α-particles (^4He-ions) transferring energy to thermal plasma during their slowing down. Only adequate confinement of α-particles and an optimised plasma scenario can provide efficient heating of the bulk plasma and steady plasma burning [1]. For this reason, plasma scenario development and fusion-born α-particle studies were some of the priorities in the second *D–T* experiments (DTE2) on the Joint European Torus (JET). JET, with its beryllium wall and tungsten divertor (known as an 'ITER-like wall') producing a significant population of α-particles with enhanced auxiliary heating systems and improved energetic-particle diagnostic capabilities, delivered these tasks [2].

Several fusion plasma devices with magnetic confinement aimed at burning deuterium-tritium plasma experiments are

[a] See Maggi *et al* 2024 (https://doi.org/10.1088/1741-4326/ad3e16) for JET Contributors.
[b] See Joffrin *et al* 2024 (https://doi.org/10.1088/1741-4326/ad2be4) for the EUROfusion Tokamak Exploitation Team.
[*] Author to whom any correspondence should be addressed.

currently under construction (ITER [3, 4], SPARC [5], Burning Plasma Experimental Superconducting Tokamak (BEST) and at the design studies (DEMO [6], STEP [7] etc). A harsh fusion reactor environment with a very high level of neutron and γ-ray fluxes will make some conventional plasma diagnostics impractical. Among the restricted set of instruments available for plasma control of burning plasmas and machine protection, neutron and γ-ray measurements can be used since they do not require direct access to the plasma and can be set up far away from the reactor vessel.

The γ-ray spectrometry of fusion plasmas [8] is based on the detection of γ-rays produced in nuclear reactions which arise in high-temperature plasmas among fast ions, fuel and impurities. On JET, γ-ray measurements were used for more than a quarter of century for diagnosing fast ions [9] and fusion-born α-particles [10–12], studying their confinement and redistribution, as well as developing the most advanced plasma scenarios [13–16]. The γ-ray spectra were recorded within the energy range 1–30 MeV. For this purpose, several γ-ray spectrometers were exploited, i.e. *BGO, NaI(Tl)* and $LaBr_3(Ce)$ scintillators and a high purity *Ge (*HP*Ge)* detector. The HP*Ge*-detector has such a high energy resolution that it allowed the analysis of the γ-line Doppler broadening [17–20]. Figure 1 represents an example of the HP*Ge*-spectrum showing the broadened γ-ray lines related to nuclear reactions due to fast ions. The $LaBr_3(Ce)$ scintillator has a very short decay-time, so the fast $LaBr_3(Ce)$ spectrometers used a fast data acquisition system that allowed measurements at MHz-counting rates [21]. JET spectrometers viewed the plasma centre vertically and tangentially [22, 23] through collimators equipped with neutron attenuators. One of the main requirements of fusion γ-ray diagnostics is the decrease of the neutrons streaming through collimators, providing substantial suppression of the γ-ray background. On JET, neutron attenuators based on ^6LiH and natural lithium composition, *LiH*, which are nearly transparent to MeV γ-rays, were used [22].

In addition, 2D γ-ray/neutron cameras [24, 25] were used to visualise the fast-ion and α-particle redistribution in plasmas due to effects related to magneto-hydro-dynamic activity and the auxiliary plasma heating with energetic neutral deuterium and tritium beam injection (NBI) and waves in the ion-cyclotron range of frequencies (ICRFs) [26–29]. It consisted of two fan-shaped array cameras with 19 collimated viewing channels (9 vertical and 10 horizontal). The importance of 2D measurements of the fast-ion γ-ray image is demonstrated in figure 2, which shows an effect of the fast ion redistribution due to the toroidal Alfvén eigenmode(TAE) instabilities in the plasma.

In JET with its carbon wall (JET-C) with some beryllium elements, carbon was the main impurity in plasmas. The resulting fast-ion diagnosis was based on measurements of γ-rays due to nuclear reactions listed in [9]. Later, in JET with its ITER-like wall (i.e. *Be*-wall and *W*-divertor), beryllium was the main impurity in plasmas and the fast-ion diagnostics were based on measurements of γ-rays generated in the $Be + p$, $Be + d$, $Be + {}^3He$ reactions [9, 20].

To study the confined ^4He-ions and fusion born α-particles, the $^9Be(\alpha,n\gamma)^{12}C$ nuclear reaction was used [12, 30–32]. Note that this diagnostic reaction was accepted as the basis for the confined α-particle measurements in the previous design of ITER [33] with a *Be*-wall. Recently, a key feature of the ITER New Baseline [34] was accepted, i.e. the use of tungsten instead of beryllium for the vessel's first wall. The fact that tungsten is more relevant for future DEMO machines and other fusion devices was taken into consideration. Initial evaluations of the new baseline and the research plan have been realised [35, 36].

In most fusion devices, glow discharge cleaning (GDC) boronisation is used for wall conditioning. Boron layers deposited on recessed surfaces getter oxygen, as well as providing high-*Z* impurity control to achieve the highest possible plasma performance [37]. Recently, it was found that solid boron injection using a dropper system [38] is a more effective method than GDC, i.e. in this case, the boron layer is long lasting on the plasma facing components, which is more relevant to fusion reactors. These boronisation methods are under consideration for application in ITER. In addition, lithium, which retains hydrogen isotopes leading to lower wall recycling, has been used to improve plasma performance [39] since *Li*-impurity reduces effective charge ($Z_{\rm eff}$) in the plasma core as well. It has been demonstrated on TFTR [40], where due to *Li*-pellet injection, a higher *D–T* fusion power at a much lower input power was achieved in super-shots compared to discharges without pellets [41]. In JET, *Ne* seeding as an extrinsic radiator strongly reduces divertor heat loads and small and high frequency ELMs. These effects were successfully demonstrated in *D–T* experiments on JET [2], providing encouraging results for ITER. This therefore acts as motivation to use *Ne* impurity for measurements of fast ions with γ-ray diagnostics as well.

Decades of intensive JET γ-ray diagnostic developments and the recent *D–T* experiments, which are verified feasibility of using γ-ray measurements for monitoring the *D–T* fusion rate and diagnosing confined α-particles, inspired us to work on this paper. Here, we propose a variety of γ-ray diagnostic applications that can be used in the present devices and during entire fusion reactor development stages, from the no- or low-activation (H/D/T/He plasmas with low neutron yield) to the burning *D–T* plasmas. Nuclear reactions generating suitable γ-rays for measurements in fusion plasmas with different low *Z*-impurities (*Li, B, C, Ne*) have been selected and recommendations for usage of these reactions based on previous experience of the γ-ray diagnostic operation on JET are provided. Gamma-ray diagnostic capabilities for all reactor exploitation phases, including the initial setup of plasma discharges, are considered as follows: detection of runaway electrons (REs) in the plasma current ramp-up and disruptions (section 2), diagnosing fast ions (*H, D, T,* ^3He) for optimising of auxiliary plasma heating systems (section 3), and optimisation of *D*- and *DT*-plasma scenarios (section 4). Possibilities of γ-ray diagnostics for α-particle studies in *D–T* and no- and low-activation plasmas are discussed in section 5.

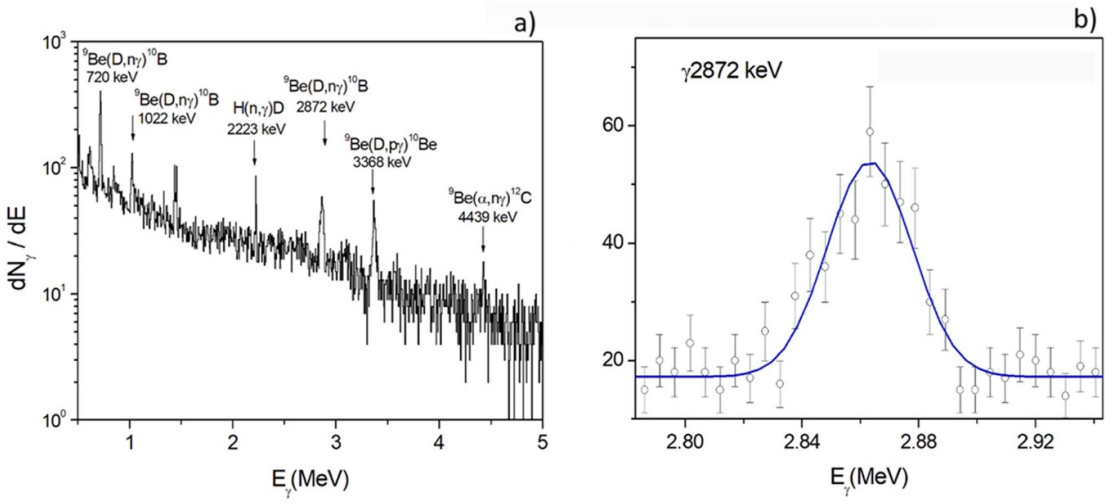

Figure 1. (*a*) Gamma-ray spectrum recorded by a HP*Ge*-detector for t = 8.5–11.5 s of JET discharge #95679. (*b*) Zoomed experimental data together with the best Gaussian fit for the Doppler broadened gamma-ray line 2872 keV from the $^9Be(D,n\gamma)^{10}B$ reaction. Reproduced from [20].

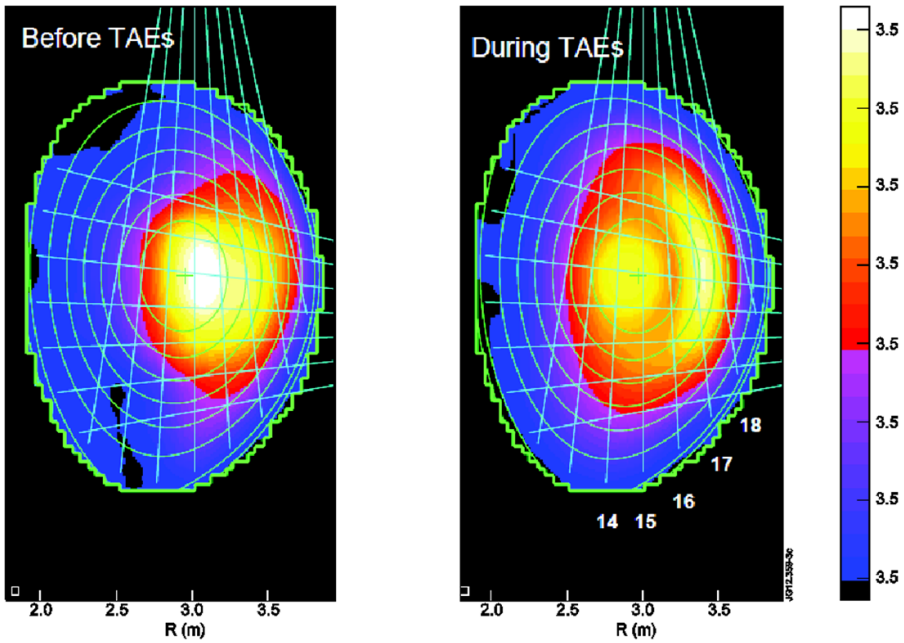

Figure 2. Tomographic reconstruction of the line-integrated intensities of 3.09 MeV γ-rays measured with γ-ray cameras: left—emissivity profile related to the period without TAE modes; right—emissivity profile observed during the TAE activity. Reproduced with permission from [28].

2. REs: start-up and disruptions

Generation of REs during the start-up phase is usual in tokamak plasma discharges. The RE formation and recipes of how it can be avoided during the JET plasma start-up have been studied [42]. With the aim of extrapolating to ITER and the cross-machine, a comparison of RE generation and the loss process during the tokamak start-up was carried out in [43]. In JET, confined REs of the order of several MeV were observed often in the start-up phase of the discharge and during fast plasma terminations due to plasma disruptions. In some cases, loss of the RE confinement led to damage of plasma facing components.

REs, interacting with plasma species and vessel materials, give rise to bremsstrahlung hard x-ray (HXR) emission as well as neutrons, if the RE energy exceeds the photonuclear reaction threshold. Therefore, basic diagnostic tools in the tokamak protection are HXR- and neutron-monitors

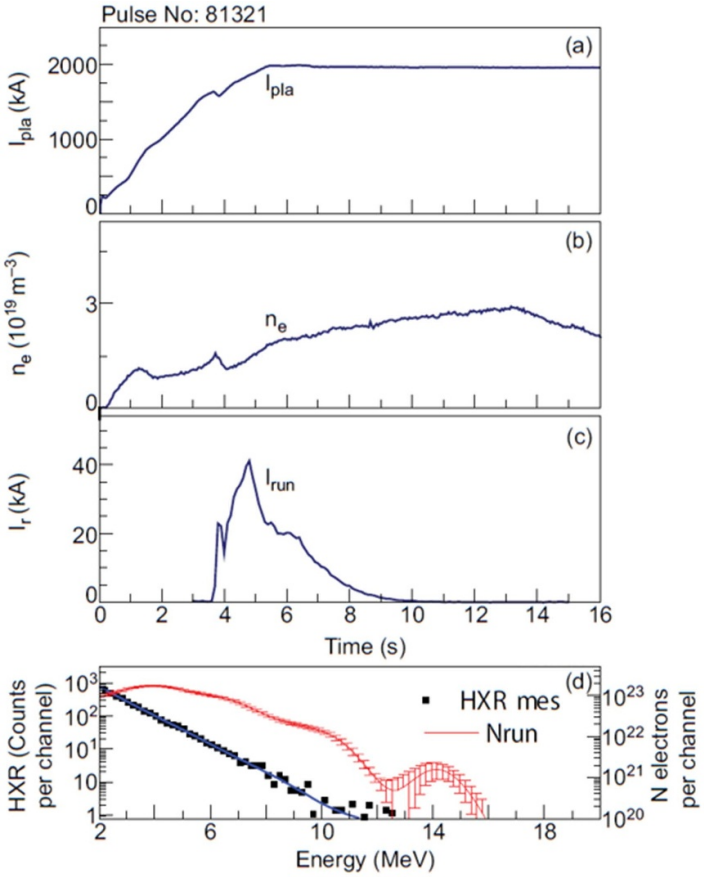

Figure 3. JET shot #81321. (*a*) Plasma current. (*b*) Plasma electron density. (*c*) Reconstructed RE current in the field of view of the γ-ray detector. (*d*) Measured HXR spectrum, $E_{HXR} > 2$ MeV (black dots), reconstructed integral RE distribution (red line) and HXR spectrum (blue line) corresponding to the reconstructed RE distribution. Reprinted from [46], with the permission of AIP Publishing.

(i.e. fission chambers), which provide waveforms indicating the appearance and development of the RE beam. However, a beneficial add-on is the installation of collimated γ-ray spectrometers, observing a specified plasma volume and recording time-dependent HXR-spectra. The HXR/γ-ray spectrometers provide information on the RE distribution dynamics [44–46], i.e. changes of the RE current and the maximal electron energy. The evolution of the confined RE beam during the JET discharge start-up [46] is shown in figure 3. HXR spectra were recorded by the γ-ray detector in the energy range $E_{HXR} > 2$ MeV. To obtain information on the RE distribution and its development during the long-lasting period, the time-dependent HXR spectra were processed with the DeGaSum code [47, 48]. This code was first developed as a tool for deconvolution of γ-ray spectra recorded for fast-ion studies in fusion plasma experiments, then subsequently upgraded to reconstruct the RE energy distribution. The reconstructed RE distributions (see figure 3(*d*)) were used to obtain the evolution of the RE current (see figure 3(*c*)) during the plasma current ramp-up. One can see that the RE current drops once the plasma current flat top is established, then slowly decreases with increasing plasma density.

Indeed, the JET experience of using γ-ray spectrometry in fusion plasma research shows that in any plasma discharge, a HXR spectrum may be recorded at the beginning of the discharge, i.e. RE appearance during a current ramp-up. Then, in the main heating phase, the γ-ray detector provides spectra related to nuclear reactions due to the presence of fast ions/α-particles in the plasma. Lastly, if a disruption breaks out in the plasma at the end of the discharge, a HXR spectrum due to REs may be recorded as well. Hence, γ-ray diagnostics can be used as a multipurpose tool for fusion plasma studies.

3. Diagnosing fast ions for optimisation of auxiliary heating systems

One of the main steps in the preparation of fusion device operation is the commissioning of auxiliary heating systems, including NBI and ICRF waves. The effectiveness of both heating systems is dictated by the specific fast-ion populations generated by these systems. Hence, the commissioning, characterisation and optimisation of heating systems benefits from the availability of good quality diagnostic data for fast ions.

Gamma rays generated in nuclear reactions between fast ions and plasma impurities and/or plasma fuel ions are used for the fast-ion identification, assessments of relative concentration and energy distribution, studying the main mechanisms of fast-ion slowing down. Two-dimensional measurements of the γ-ray emission allow us to visualise fast ions

in plasmas, monitoring their redistribution and losses, thus providing important information, in addition to conventional diagnostics, for the development of optimal plasma scenarios with auxiliary plasma heating.

The JET NBI system [49, 50] had two neutral injector boxes each with eight positive-ion neutral injectors (PINIs) which worked with H_2, D_2, T_2, and *He* gases. These PINIs, with a maximum *D*-beam injected power of 2.2 MW, were operated with energies up to 125 keV. This beam energy was not sufficient to use γ-ray measurements for diagnosing NBI ions. However, high-energy negative-ion-source based NBI (N-NBI) systems can provide more energetic beams, thereby making γ-ray diagnostics suitable for their detection. For example, the Large Helical Device (LHD) is already exploiting the *H*-beam with energy up to 190 keV. Furthermore, the commissioning of two 5-MW N-NBI units with a beam energy of 500 keV is planned on the JT-60SA tokamak. In ITER, N-NBI beams (hydrogen and deuterium) with energies up to 1 MeV will also be implemented in the future.

It is important to characterise NBI heating using all available beam-plasma combinations, i.e. *H*-beam into *H-, D-, T-* and *He*-plasmas, and *D*-beam into *H-, D-* and *T*-plasmas. Information on the beam power deposition, shine-through etc can help the development of plasma scenarios for burning plasmas and studying new physics due to the high energy beam–plasma interactions. Indeed, recent measurements of the beam-driven Alfvén eigenmode (AE) activity in DIII-D plasmas with reversed magnetic shear [51], showed a large difference in the driven mode amplitudes injecting *H-* or *D*-beams in mixed background plasmas (*D–H*).

ICRF heating commissioning begins with the optimisation of the RF coupling at available frequencies to achieve the best heating efficiency varying gas injection, antenna phasing, etc. On JET, where the ICRH system was commissioned in the frequency range $f = \omega/(2\pi) \approx$ 23–57 MHz, γ-ray diagnostics provided a lot of insightful data. Indeed, the energetic ion-tail due to ICRH, in some cases in the MeV-range, gave rise to nuclear reactions resulting in an intensive γ-ray emission from the plasma. It is important to start the ICRF heating setup in the non-/low-activation *H-, D-, T*-plasmas, using various heating schemes which generate energetic *H-* and ^{3}*He*-ions. In these plasmas, due to the low level of the neutron-induced background, a comprehensive set of diagnostics can be employed which is significantly limited during the *D–T* plasma operation.

3.1. Optimisation of ICRF heating systems generating energetic ^{3}He-ions

ICRF heating scenarios using ^{3}*He* are rarely used for system commissioning. Yet these scenarios have a range of applications in fusion research, including maximising bulk ion heating and various fast-ion studies. In view of the scenario development for *D–T* plasmas, often scenario elements are first tested in *H-, D-* and *H–D* plasmas.

There are several ICRH scenarios, where a small amount of ^{3}*He*-ions is used to absorb the ICRH power. In deuterium plasmas, ^{3}*He*-minority heating is , typically, the most optimal at $n_{3He}/n_e \sim$ 5%–10%, while lower concentrations, $n_{3He}/n_e \sim$ 2%–3% optimise the heating in hydrogen plasmas. The typical energies for ICRF-generated ^{3}*He*-ions vary from ∼50–100 keV to MeV-range energies, depending on the minority concentration, ICRF heating power and phasing, plasma density and other parameters. The experiment parameters are usually adjusted to maximise or limit the fast-ion energies, depending on the specific target application of ICRF waves. The three-ion *D–*(^{3}*He*)*–H* and ^{4}*He–*(^{3}*He*)*–H* ICRH scenarios with very low ^{3}*He* concentrations (<0.5%) are particularly relevant for fast-ion applications in predominantly hydrogen plasmas (with ∼10%–30% of deuterium or ∼5%–15% of ^{4}*He*). These scenarios could be relevant for SPARC and, as discussed in [36] for the SRO phase of ITER, as an opportunity for early tests of energetic particle modelling and diagnostics.

The selected nuclear reactions for γ-ray diagnosing energetic ^{3}*He*-ions are presented in table 1.

On JET, in the scenario with fundamental ^{3}*He*-minority and mode conversion (MC) wave heating at f ≈ 32 MHz, fast ^{3}*He*-ions accelerated by ICRH in the MeV-energy range were detected in discharges with a low ^{3}*He*-concentration in the *H-* and *D*-plasmas. In view of the foreseen ICRF heating operation in the non-activated ITER phase, the examination of ^{3}*He* fundamental minority heating performance in *H*-plasmas is in demand. ICRF heating of *H*(^{3}*He*) plasmas was carried out at half the nominal ITER magnetic field, 2.65 T, which mimics the RF wave absorption at f ≈ 52 MHz in *D–T* plasmas [52]. The main indicator of the fast ^{3}*He*-ion generation was γ-rays from the reaction *D*(^{3}*He*,γ)^5*Li* in the case of *D*-plasmas, and ^{9}*Be*(^{3}*He*,*p*γ)^{11}*B*, ^{12}*C*(^{3}*He*,*p*γ)^{14}*N* reactions in *H-, D*-plasmas due to beryllium and carbon which were the main JET impurities [9, 16].

D(^{3}*He*,γ)^5*Li reaction*. In deuterium JET plasmas, this reaction was a major diagnostic reaction for the characterisation of ICRF heating and fast-ion studies in experiments with ^{3}*He*-minority. It is a weak γ-ray branch of the aneutronic fusion reaction *D*(^{3}*He*,*p*)^4*He*, Q = 18.353 MeV which, producing a 3.6 MeV α-particle and 14.7 MeV proton, has a pronounced resonance in the cross-section, $\sigma \approx 0.81$b, at the ^{3}*He* energy $E_{3He} \approx 0.67$ MeV [53]. According to measurements made in [54], the branching ratio of these reactions is $\Gamma_\gamma/\Gamma_p \approx 5 \times 10^{-5}$ in the centre-mass energy range 25–60 keV (here, $\Gamma = \hbar/\tau$ is a quantum mechanics parameter related to the probability of an event). However, this ratio increases at higher energies, reaching $\sim 10^{-3}$ in the MeV-range [55, 56]. As long as the intrinsic widths of the ^{5}*Li* ground and first excited states are $\Gamma_0 \approx 1.5$ MeV and $\Gamma_1 \approx$ 3–6 MeV, the gamma-rays, γ_0 ($E_{\gamma 0} \approx 17$ MeV) and γ_1, corresponding to transitions to these states, cannot be resolved in the measured spectra with reasonable accuracy. This reaction can therefore be used for relative reaction rate measurements only, providing information

Table 1. Diagnostic nuclear reactions for characterisation of fast ^3He-ions.

Reaction	Energy of reaction, Q (MeV)	Energy of gammas, E_γ (MeV)	Reaction application comments
$D(^3He,\gamma)^5Li$	16.66	17	D-plasma; ICRH performance; α-particles production; $E_{Res} \approx 0.65$ MeV
$T(^3He,\gamma)^6Li$	15.795	2.186, 3.563 & γ_0, γ_1, γ_2	T-plasma
$^7Li(^3He,\gamma)^{10}B$	17.788	0.718, 2.868, 3.586, 4.055 & γ_0, γ_1, γ_4, γ_5	Low-activation plasmas; $E_{Res} \approx 0.92$, 1.45, 2.16 and 3.45 MeV
$^{11}B(^3He,pn\gamma)^{12}C$	8.239	4.44, 3.21 & 9.64	Low-activation plasmas
$^{12}C(^3He,p\gamma)^{14}N$	4.779	1.635, 2.313, 2.793, 4.914 & 5.106 etc	C-impurity
$^{20}Ne(^3He,p\gamma)^{22}Na$	5.782	0.583, 0.891, 2.211, 2.968 and 3.059 MeV	Low-activation plasmas

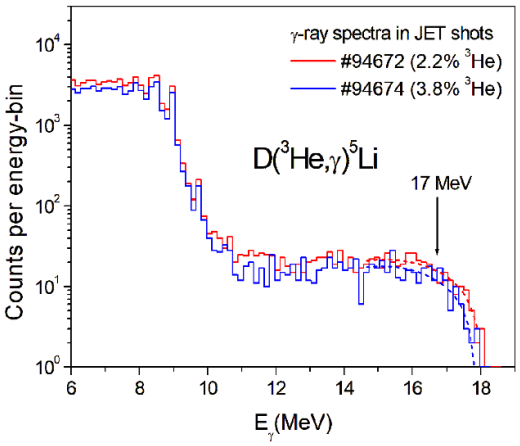

Figure 4. Comparison of γ-ray spectra from $D(^3He,\gamma)^5Li$ reaction recorded from ICRF heated plasmas with different ^3He-concentrations.

on changes of the plasma's heating efficiency. Figure 4 shows spectra recorded in two similar deuterium plasma discharges with ^3He-minority ICRF heating but with different ^3He concentrations. One can see that the γ-ray count rate is higher at 2.2% concentration than at 3.8%, indicating the presence of more energetic ions which is increasing the fusion reactivity $<\sigma v_{3He}>$ at lower ^3He concentration. Information on other diagnostic reactions producing γ-rays, i.e. ^3He reactions with intrinsic low-Z impurities, the likes of carbon, boron, lithium etc can help with complete characterisation of the ^3He-ion distribution function.

$^{12}C(^3He,p\gamma)^{14}N$ reaction. Before the ITER-like wall upgrade, this reaction was rather practical for the characterisation of ICRF accelerated ^3He-ions in JET H- and D-plasmas. The excitation functions of the ^{14}N states [57] represented in figure 5 have been used to assess the ^3He-ion energy distribution function [8, 16, 19]. The ^3He-ions with $E_{3He} > 1.5$ MeV populate the ^{14}N excited states [58] shown in this figure. The most intensive γ-ray transitions 1.635, 2.313, 2.793, 4.915 and 5.106 MeV are useful for the ^3He-ion energy distribution analysis. In the case of the very energetic ^3He-ion tail, several high-energy states could be excited (in figure 5, the excitation energy related to $E_{3He} = 3$ MeV is shown). It is important to emphasise that the synergy of γ-ray analysis of both $^{12}C(^3He,p\gamma)^{14}N$ and $D(^3He,\gamma)^5Li$ reactions provide a diagnostic advantage for the fast ^3He-ion characterisation in fusion plasma devices with carbon impurity.

$^{11}B(^3He,pn\gamma)^{12}C$ reaction. Boron doping provides an opportunity to monitor the MeV ^3He-ions in metallic-wall devices, i.e. without carbon and beryllium plasma-facing components. Evaluated cross-sections of the strongest $^{11}B + {}^3He$ reactions are shown in figure 6. It is clearly shown that the yield of the $^{11}B(^3He,pn\gamma)^{12}C$ reaction is an order of magnitude higher than that of other reactions. According to the scheme of the ^{12}C excited states shown in figures 6, ^3He-ions with energy $E_{3He} \sim 1$ MeV give rise to 4.440 and 3.214 MeV gammas. However, more ions (several MeV energy) could excite the level 9.641 MeV as well, which is de-excited by the transition to the ground state, as shown in figure 6. Indeed, in the high-performance D-plasma, the D–D fusion products, 3 MeV protons, 1 MeV tritons and 0.82 MeV ^3He-ions, are heavily generated, so the secondary reactions with them, $^{11}B(p,\gamma)^{12}C$ and $^{11}B(t,2n\gamma)^{12}C$, are giving rise to the ^{12}C gammas that could confuse the characterisation of ^3He-ions. Therefore, it is recommended to use this reaction in H-, HD-, H^4He- and T-plasmas. In T-plasmas, the bulk tritium can be accelerated during the ^3He-ion heating due to the second harmonic coupling; nevertheless the T-tail is low-energetic and the $^{11}B(t,2n\gamma)^{12}C$ reaction should not affect the $^{11}B(^3He,pn\gamma)^{12}C$ reaction analysis.

$^7Li(^3He,\gamma)^{10}B$ reaction. Doping the plasma with a small amount of lithium could be beneficial for the characterisation of the ^3He in ICRF heating scenarios, especially those which are generating MeV ^3He-ions. This is an additional option for

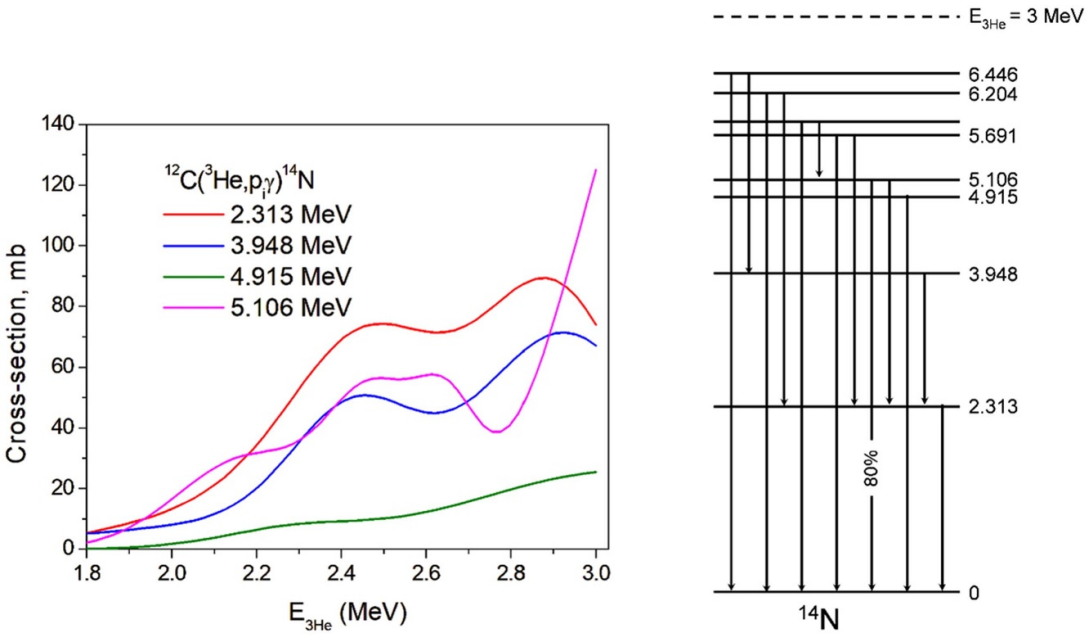

Figure 5. Excitation functions of the ^{14}N states [57] and the ^{14}N level scheme with strongest γ-ray transitions [58]; 5.1 MeV transition branching ratio (%) is shown, and the dash level indicates the energy excitation of ^{14}N by 3 MeV ^3He-ions.

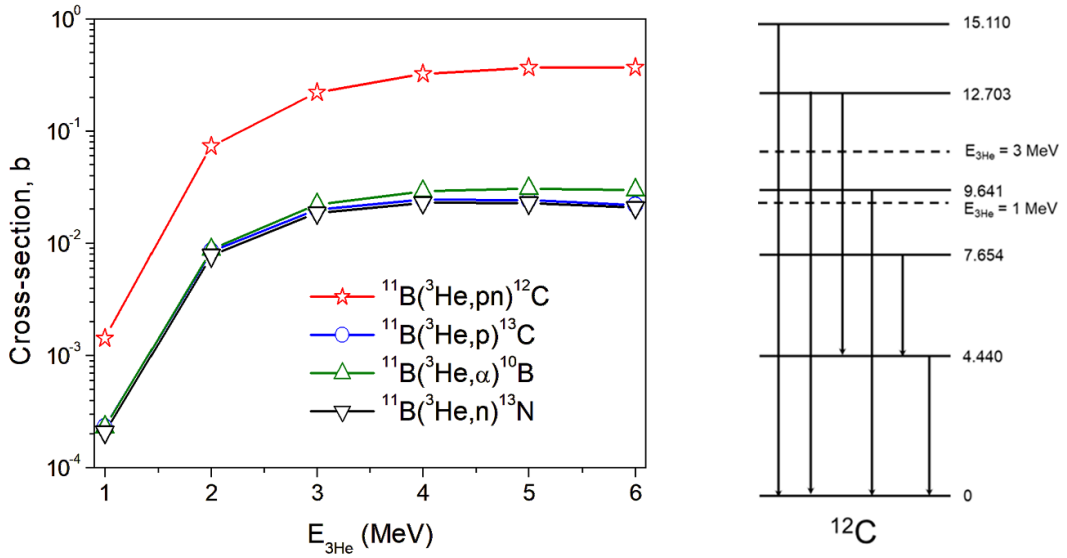

Figure 6. Evaluated total cross-sections of $^{11}B(^3He,X)$ reactions and scheme of the ^{12}C excited states with transitions between them [58]; dash lines correspond to excitation energies related to 1- and 3 MeV ^3He-ions.

the characterisation of fast ^3He-ions. Several resonances are found in this radiation capture reaction. From the diagnostics' point of view, the most useful resonances are at $E_{3He} \approx 0.92$ ($E^*_{10B} \approx 18.43$ MeV), 1.45 (18.8), 2.16 (19.3) and 3.45 (20.2) MeV [59]. The decay of the ^{10}B resonant states with energies E^*_{10B} mainly goes to the ground state (γ_0), 1st (γ_1), 4th (γ_4) and 5th (γ_5) excited states (see figure 7(*a*)). Energies of the transitions are defined as $E_{\gamma i} \approx E^*_{10B} - E_i$. Since the resonant states have an intrinsic width, the related peaks are rather broad. Thus, there are high- and low-energy peaks in the γ-ray spectrum for the ^3He-ion heating analysis, i.e. a number of the broad overlapped γ-ray peaks in the energy range 13–20 MeV and several monochromatic γ-ray lines below 5 MeV. Both energy regions of the $^7Li(^3He,\gamma)^{10}B$ reaction γ-ray spectrum are extremely sensitive to the ^3He-ion energy tail (see figure 7(*b*)) which is important for the analysis of the ICRH heating. It is important to note that in the *D*- and *T*- plasmas, the high-energy gammas related to resonance transitions in the

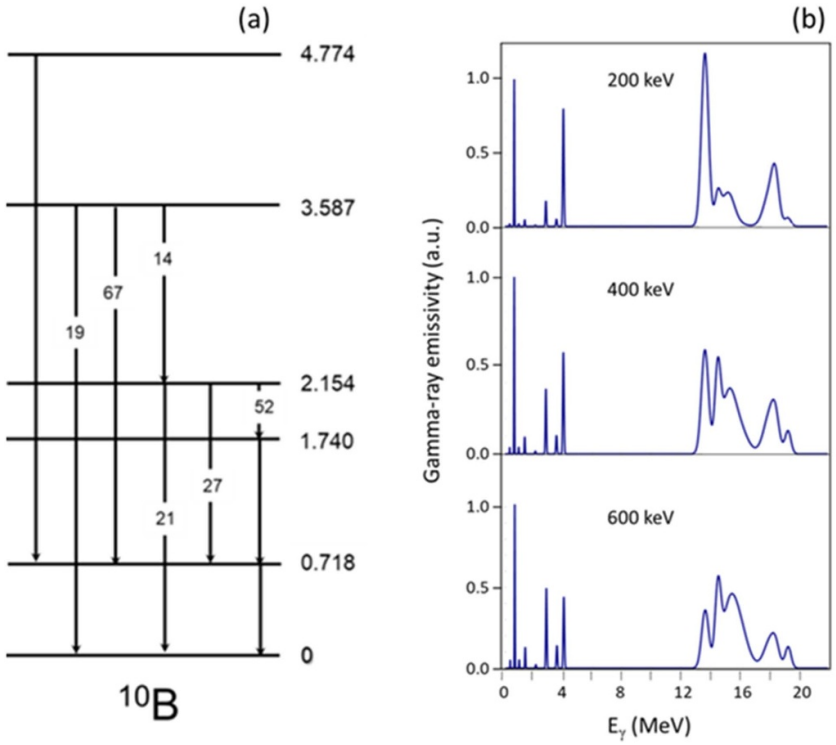

Figure 7. (*a*) Scheme of the ^{10}B excited states and transitions between them [58]; level energies (MeV) and transition branching ratios (%) are shown. (*b*) Emission spectra of γ_0, γ_1, γ_4, γ_5 gammas and related low-level γ-ray transitions from $^{7}Li(^{3}He,\gamma)^{10}B$ reaction calculated for different ^{3}He-ion Maxwellian tails at temperature $T_{3He} =$ 200, 400 and 600 keV.

$^{7}Li(^{3}He,\gamma)^{10}B$ reaction could cause a problem for the analysis of other γ-rays, i.e. 17 MeV from $D(^{3}He,\gamma)^{5}Li$ and ≈20 MeV from $T(^{3}He,\gamma)^{6}Li$) reactions, in the same ^{3}He energy range.

$T(^{3}He,\gamma)^{6}Li$ reaction. In the big-bang nucleosynthesis in the early Universe, this reaction is hypothesised to have contributed to ^{6}Li production. For studies in tritium plasmas, it can be used to characterise ^{3}He-ions with energies exceeding 0.5 MeV, such that no extra plasma impurities are needed for γ-ray diagnosing. The capture of γ-rays of the $T(^{3}He,\gamma)^{6}Li$ reaction (Q = 15.795 MeV) to the ground state of ^{6}Li, γ_0, as well as the first and second excited states, γ_1 (E_1 = 2.186 MeV) and γ_2 (E_2 = 3.563 MeV), have been observed for $E_{3He} > 0.5$ MeV [60]. Energies of these gammas can be defined as $E_{\gamma i} \approx Q + (1/2)E_{3He} - E_i$. Figure 8(*a*) represents measured excitation functions of this reaction [61]. It was found that the capture of the γ-ray emission spectrum is sensitive to the ^{3}He-ion energy distribution. The demonstration of this sensitivity is presented in figure 8(*b*), where emission spectra were calculated, using available data and a Maxwellian ^{3}He-ion distribution with different temperatures. Note that the population of the low-lying states leads to the appearance of 2.186 MeV and 3.563 MeV γ-rays that can also be used for ^{3}He-ion diagnosis.

If neon is injected as an extrinsic radiator in the low-activation plasma, the $^{20}Ne(^{3}He,p\gamma)^{22}Na$ reaction (Q = 5.782 MeV) can be used for the optimisation of the ICRF heating. However, the ^{3}He-ion tail needs to be rather energetic because of the high Coulomb barrier for the ions. The cross-section of this reaction increases rather fast with the energy of the ^{3}He-ions, e.g. it is ∼0.5 mb at E_{3He} = 2 MeV and ∼100 mb at 4 MeV [58]. This reaction generates γ-rays in the energy range of the intensive neutron-induced γ-ray emission. Thus, the $^{20}Ne(^{3}He,p\gamma)^{22}Na$ reaction can be used for diagnosing ^{3}He-ions in low-activation plasmas.

Remarks. The observation of 17 MeV gammas from the $D(^{3}He,\gamma)^{5}Li$ reaction is a main indicator of the fast ^{3}He-ions in deuterium plasmas. In devices with boronisation, the $^{11}B(^{3}He,pn\gamma)^{12}C$ reaction is useful in low-activation plasma experiments, while in machines with unavoidable carbon impurities (e.g. JT-60SA), the $^{12}C(^{3}He,p\gamma)^{14}N$ reaction could be practical.

3.2. Characterisation of heating systems generating energetic H-ions

Energetic *H*-ions can be generated with both NBI and ICRF heating systems. The energy range for *H*-ions generated with NBI depends on the plasma source technology for the NBI system. In JET and present-day devices, positive-ion NBI technology is commonly used, providing *H*-ions in the energy range ∼50–110 keV in the plasma. In future tokamaks, neutral beam injection systems with a negative-ion-source (N-NBI) will provide more energetic *H*-ions to the plasma. For example, the N-NBI systems for JT-60SA and ITER are designed to deliver

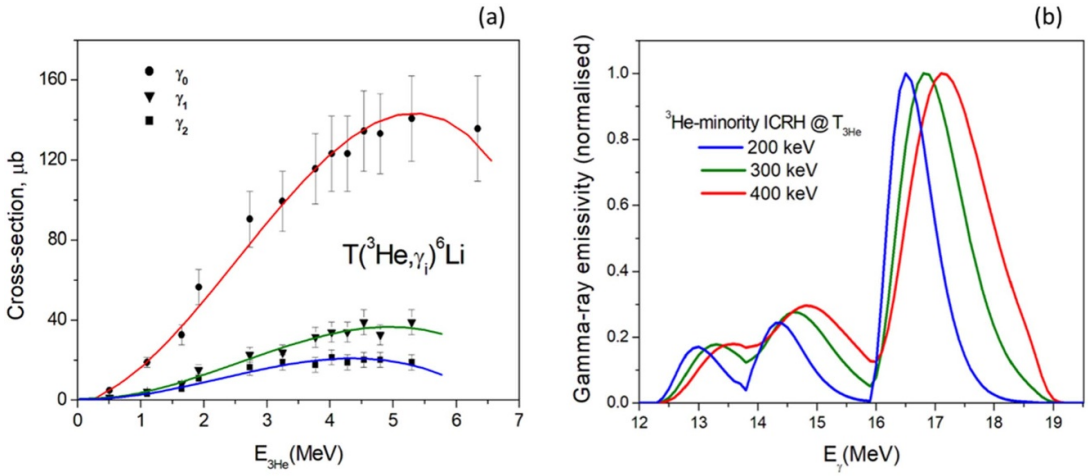

Figure 8. (*a*) Cross-sections of the *T(^{3}He,γ)^{6}Li* reaction measured for the capture gammas γ_0, γ_1 and γ_2 [61]. (*b*) Capture of γ-ray emissivity from the *T(^{3}He,γ)^{6}Li* reaction calculated for different *^{3}He*-ion Maxwellian tails at temperature T_{3He} = 200, 300 and 400 keV.

fast *H*-ions with energies up to 500 keV and 870 keV, respectively. In the LHD, these ions are accelerated up to 190 keV.

In the case of ICRF heating, the energy range for fast *H*-ions can vary from ∼50 to 100 keV up to a few MeV depending on many factors, including available heating power, the ICRH scenario and plasma density. Hydrogen minority heating with ICRF waves is the widely-used scenario for plasma heating of *D*-, *T*- and *DT*-plasmas. The advantage of this scenario is the good performance over a wide range of hydrogen concentrations (typically ∼3%–10%). For example, in JET experiments in [9], the hydrogen tail was accelerated up to 5 MeV. Typically, *H*-minority heating produces ions in the range of a few hundred keV to 1–2 MeV. For heating experiments in hydrogen plasmas, the second harmonic has also been applied. The application of this ICRH scenario is usually associated with generating MeV-range *H*-ions in the plasma. Diagnostic information on *H*-ion energies in the plasma is important for both NBI and ICRH systems, e.g. in view of accurate shine-through and hot-spot validation. Furthermore, it provides valuable data for adjusting and optimising the heating systems within the operational boundaries to deliver the projected system performance, following the commissioning stage. Selected nuclear reactions for γ-ray diagnosis of energetic *H*-ions are presented in table 2.

In JET, the main source of energetic *H*-ions in the MeV-energy range was ICRF heating. The energetic *H*-ion tail was characterised using γ-rays from *D(p,γ)^{3}He*, *^{9}Be* + *p* reactions and *^{12}C* + *p* inelastic scattering [9].

D(p,γ)^{3}He reaction. This radiation capture reaction is a very important diagnostic tool, which can be used for transport studies of *H*-ions in deuterium and *D*-ions in hydrogen plasmas. The first observation of this reaction in a tokamak plasma by means of measurements of 5.5 MeV gammas was at Doublet-III (DIII-D) in 3.6 MW NBI (E_H < 70 keV) heated discharges during 0.2 s [62]. It was a big challenge because the reaction cross-section at these energies is below 0.3 μb [63–65]. In the case of the hydrogen NBI heating in ITER, the yield of these γ-rays could be much higher as the cross-section grows rapidly, reaching ≈4 μb at E_p = 1 MeV [66]. During *H*-minority ICRF heating, an effective temperature of the *H*-ion energetic tail can be inferred with the *D(p,γ)^{3}He* reaction. An example of the 5.5 MeV γ-ray spectrum and energy distribution assessments in JET experiments [9] is presented in figure 9. The analysis of the recorded capture γ-ray peak was made using the Maxwellian tail approximation for the energy distribution; it was found that ICRH accelerated *H*-ions had $T_H \approx$ 200 keV. Note that the astrophysical approach using the Gamov peak definition [67] is not valid for T_H > 100 keV; physically, the capture γ-ray peak depends on the maximum overlap of the tail distribution, which decreases at high *H*-ion energies, and the reaction cross-section that increases with their energy. The sensitivity of the capture γ-ray peak to the *H*-ion energy distributions during the *H*-NBI and *H*-minority ICRF heating is demonstrated in figure 10. In the NBI case, the 5.5 MeV γ-ray spectrum depends on T_e due to energetic *H*-ions mostly slowing down on electrons. The line-integrated electron temperature can therefore be specified with these measurements. The *H*-ion ICRH distribution tail also depends on T_e, however the 5.5 MeV γ-ray spectrum depends more strongly on the effective T_H. One can see that the 5.5 MeV peak is rather broad in both the NBI and ICRF plasma heating scenarios. According to the JET experience, the use of the *D(p,γ)^{3}He* reaction for *H*-ion diagnosis has some restrictions. It could be unsuitable for NBI characterisation at E_{NBI} < 100 keV as the 5.5 MeV γ-ray yield is not sufficient for reliable measurements. In the case of ICRF heating, it can be difficult to separate 5.5 MeV γ-rays from the detected γ-ray background if the tail temperature T_H > 400 keV because the peak becomes too broad. In addition, selecting the γ-ray detector line-of-sight, one needs to consider the high recoil velocity of the *^{3}He** nucleus that leads to a significant Doppler effect for the 5.5 MeV γ-rays emitted.

Table 2. Diagnostic nuclear reactions for characterisation of energetic *H*-ions.

Reaction	Energy of reaction, Q (MeV)	Energy of gammas, E_γ (MeV)	Reaction application comments
$D(p,\gamma)^3He$	5.49	5.5	*D*-plasma; ICRH, $T_H < 400$ keV *D*-plasma; NBI, $E_H > 100$ keV
$T(p,\gamma)^4He$	19.814	20	*T*-plasma; ICRH, $T_H > 50$ keV *T*-plasma; NBI, $E_H > 100$ keV
$^7Li(p,\gamma)^8Be$	17.255	γ_0, γ_1, γ_3, γ_4	Low-activation plasmas; $E_{res} \approx 0.44$, 1.03, 1.89, 2.06 MeV
$^{11}B(p,\gamma)^{12}C$	15.957	4.44 & γ_0, γ_1	Low-activation plasmas; $E_{Res} \approx 0.163$ MeV
$^{10}B(p,p_i\gamma)^{10}B$	—	0.718, 1.74 etc	Low-activation plasmas; $E_p > 0.8$ MeV $E_p > 2.6$ MeV
$^{11}B(p,p_i\gamma)^{11}B$		2.125, 4.445 etc	
$^{12}C(p,\gamma)^{13}N$	1.9435	γ_0: 2.365, 3.502	Low-activation plasmas, *C*-impurity; $E_{Res} \approx 0.458$ & 1.7 MeV
$^{12}C(p,p_i\gamma)^{12}C$	—	4.44, 3.21 etc	*C*-impurity; *D*-, *T*-plasmas ICRH, $E_p > 4.85$ MeV
$^{22}Ne(p,\gamma)^{23}Na$	8.794	γ_i & 0.440, 2.288, 2.541, 3.237, 3.325 3.915	Low-activation plasmas; $E_{Res} \approx 0.436$, 0.479, 0.639, 0.661 & 1.279 MeV

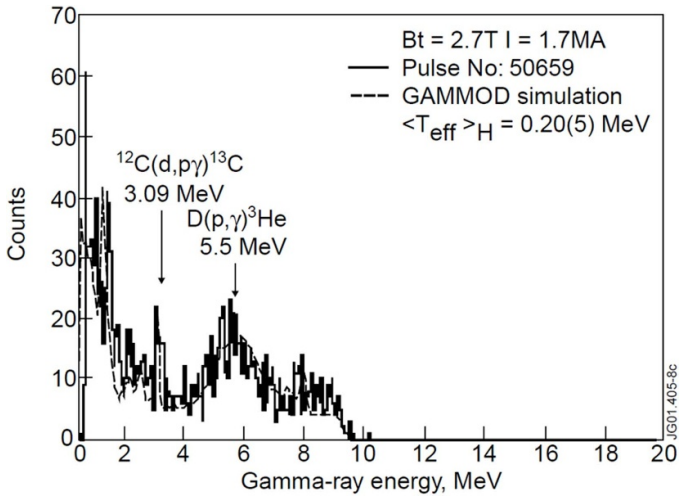

Figure 9. Gamma-ray spectrum recorded during 1.7 MA/2.7 T discharge with *H*-minority ICRF heating in deuterium JET plasma; the GAMMOD code [9] analysis of the 5.5 MeV γ-ray peak provided an effective temperature of the *H*-ion tail—the second harmonic acceleration of deuterium was identified due to the appearance of characteristic 3.09 MeV gammas from the $^{12}C(d,p\gamma)^{13}C$ reaction. Reproduced from [9]. © 2002 IAEA, Vienna. Published under licence by IOP Publishing Ltd. All rights reserved.

$T(p,\gamma)^4He$ reaction. In tritium and DT-plasmas, the detection of 20 MeV capture γ-rays is extremely important for both NBI and ICRF heating scenarios with energetic *H*-ions. The first measurements of this reaction in plasma experiments were carried out on JET. Figure 11 represents 20 MeV γ-ray spectra recorded by vertical and tangential JET spectrometers in discharges with *H*-minority heating of tritium plasmas [12]. In the first approximation, using the Maxwellian tail approximation and reaction cross-sections for $E_p < 80$ keV [68] and $E_p = 0.1$–6.0 MeV [69], it was found that $T_H < 400$ keV. Calculations performed similarly to those for the $D(p,\gamma)^3He$ reaction (see figure 12) show that the 20 MeV capture γ-ray peak can be used to infer the *H*-ion energy distributions, as well as T_e during the *H*-NBI and *H*-minority tail temperature with ICRF heating. Note that the neutron induced γ-ray background is very low in the range $E_\gamma > 9$–10 MeV in deuterium/tritium and $E_\gamma > 15$ MeV in *D*–*T* plasmas. This is a big advantage in making measurements of 20 MeV γ-rays from the $T(p,\gamma)^4He$ reaction for the characterisation of the plasma heating.

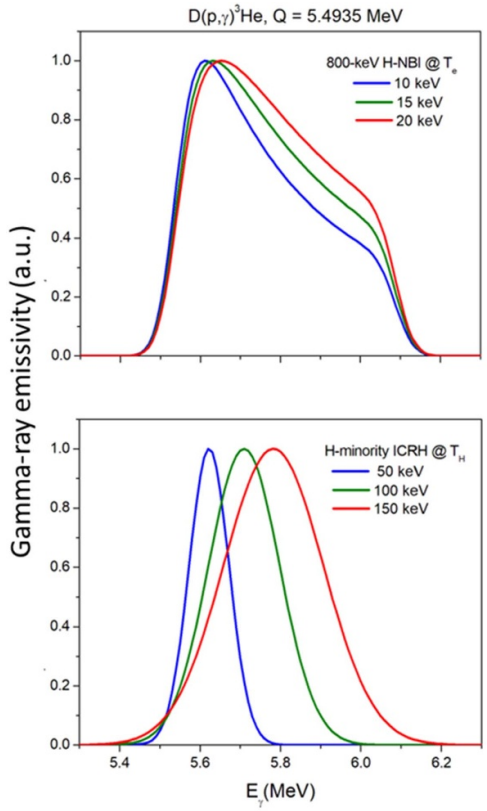

Figure 10. Calculated 5.5 MeV γ-ray emissivity due to $D(p,\gamma)^3He$ reaction. Top figure—spectra related to 800 keV hydrogen NBI heating deuterium plasmas with electron temperatures 10, 15 and 20 keV. Bottom figure—spectra related to *H*-minority ICRF heated with Maxwellian tail temperatures 50, 100 and 150 keV.

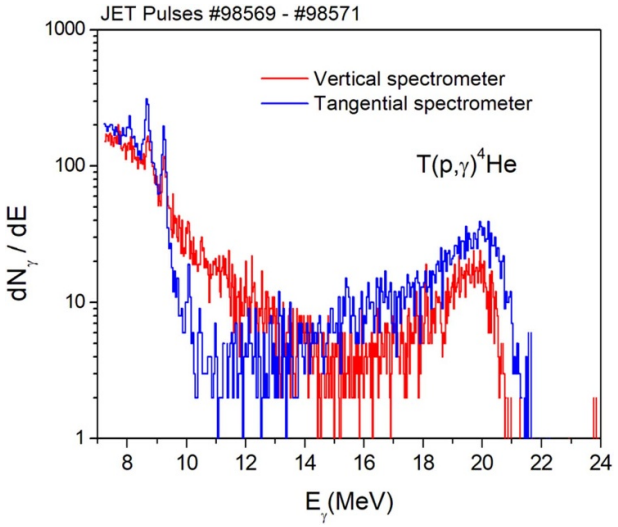

Figure 11. Gamma-ray spectra recorded by vertical and tangential spectrometers during 1.8 MA/2.2 T discharge with H-minority ICRF heating of tritium plasma in JET; 20 MeV γ-rays from the $T(p,\gamma)^4He$ reaction were observed. Reproduced from [12]. © 2024 The Author(s). Published by IOP Publishing Ltd on behalf of the IAEA. CC BY 4.0.

$^7Li(p,\gamma)^8Be$ reaction. In the case of lithium injection, this reaction is helpful for the characterisation of the *H*-NBI heating of the *H*-plasma and *H*-minority ICRF heating in *D*-plasmas. Several resonances in the excitation function of $^8Be^*$

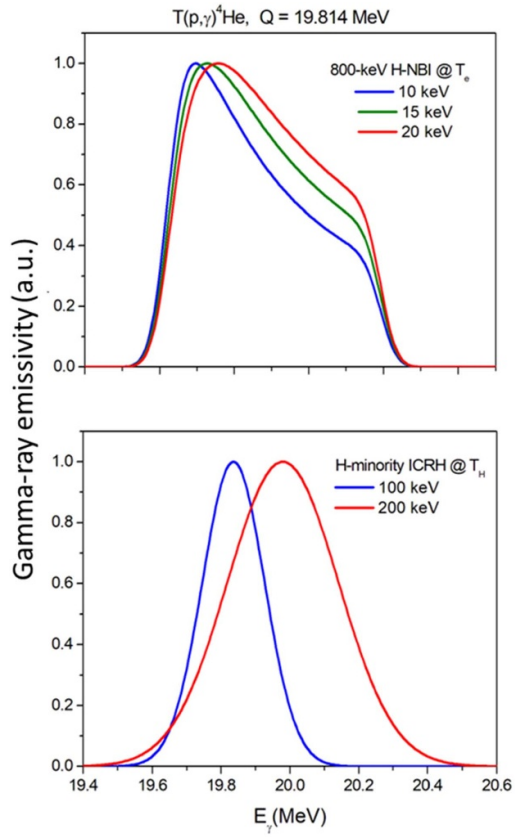

Figure 12. Calculated 20 MeV γ-ray emissivity due to $T(p,\gamma)^4He$ reaction. Top figure—spectra related to 800 keV hydrogen NBI heating tritium plasmas with electron temperatures 10, 15 and 20 keV. Bottom figure—spectra related to *H*-minority ICRF heating with Maxwellian tail temperatures 100 and 200 keV.

by the $^7Li(p,\gamma)^8Be$ reaction are known [58], i.e. resonances at the proton energies $E_p \approx 0.44$, 1.03, 1.89 and 2.06 MeV. The associated resonant states of $^8Be^*$ at $E_{8Be} \approx 17.64$, 18.15, 18.9 and 19.07 MeV are mostly de-exciting by γ_0, γ_1, γ_3 and γ_4 transitions (see figure 13(*a*)). The resonance at $E_p \approx 0.44$ MeV can be used for *H*-NBI characterisation in *H*-plasmas. In this case, high-energy γ-rays, $E_{\gamma 0} \approx 17.64$ MeV and $E_{\gamma 1} \approx 14.59$ MeV, appear in the γ-ray spectrum. Note that the absence of the neutron-induced background in *H*-plasmas also allows the detection of low-energy gammasin particular, at energies ≈1.014 MeV and ≈0.718 MeV, related to transitions to 16.63 and 6.92 MeV levels. At $E_p < 0.44$ MeV, the analysis of captured γ-rays resulting from γ_0 and γ_1 transitions could provide additional information on the energy distribution of NBI *H*-ions. Characterisation of *H*-ions accelerated during the ICRF heating of *D*-plasmas can be done by measuring γ_0 and γ_1 transitions from all known resonances. Gamma-ray peaks related to the γ_1 transition to the first excited state $E_1 \approx 3.03$ MeV are rather broad because of the intrinsic width $\Gamma_1 \approx 1.5$ MeV. However, using high-efficiency detectors [70], overlapping of the γ-ray peaks related to different resonances can be resolved because of a low neutron-induced background in the γ_1 energy range. Figure 13(*b*) represents the calculation results of the $^7Li(p,\gamma)^8Be$ reaction γ-ray emissivity in the Maxwellian tail approximation. One can see that the γ-ray

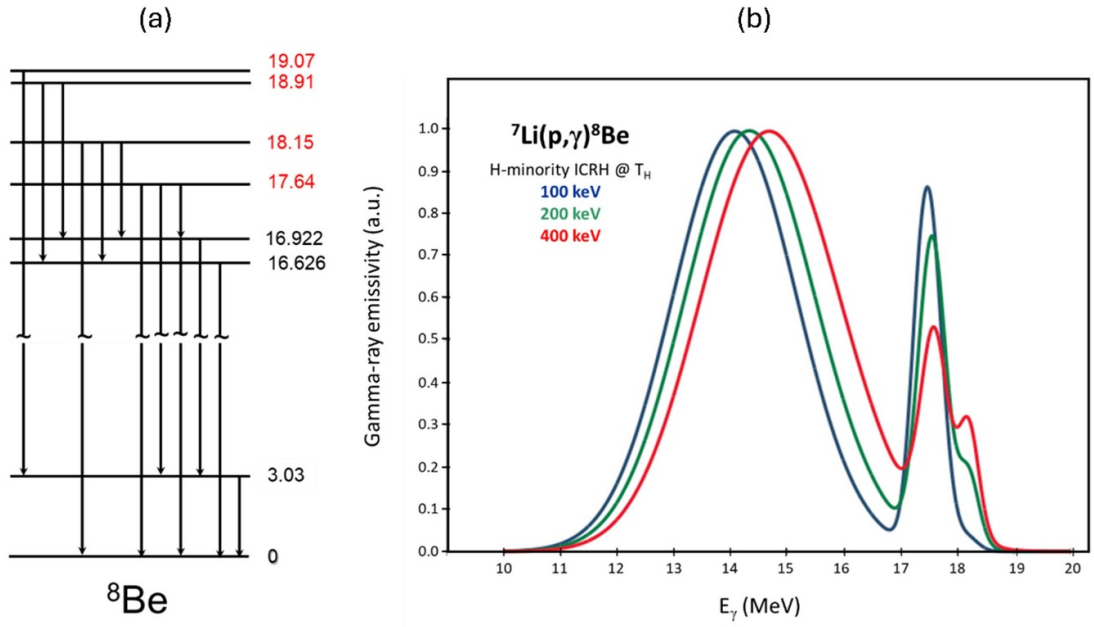

Figure 13. (*a*) Scheme of the ^{8}Be levels; $^{7}Li(p,\gamma)^{8}Be$ reaction resonant states highlighted in red. (*b*) Calculated γ-ray emissivity due to the $^{7}Li(p,\gamma)^{8}Be$ reaction; the colour coded γ-ray spectra are related to different Maxwellian tail temperatures, T_H.

spectrum strongly depends on the effective *H*-ion temperature, T_H. The $^{7}Li(p,\gamma)^{8}Be$ reaction can therefore be useful for the characterisation of the ICRF plasma heating.

$^{11}B + p$ reactions. The interaction of energetic protons with boron can also play an important role for the characterisation and optimisation of the NBI and ICRF heating systems with γ-ray diagnostics. One of the advantages of the capture reaction $^{11}B(p,\gamma)^{12}C$ is that the lowest proton reaction resonance takes place at $E_p = 0.162$ MeV. Note that this reaction is a branch of the $^{11}B(p,2\alpha)^{4}He$ reaction known as the 3-alpha aneutronic fusion reaction, which has a very high cross-section, $\sigma \approx 1.4$ b at $E_p \approx 0.65$ MeV [71]. The $^{11}B(p,\gamma)^{12}C$ resonant state decays with γ_0 and γ_1 transitions, $E_{\gamma 0} = 16.11$ MeV and $E_{\gamma 1} = 11.67$ MeV. The cross-sections of these resonance transitions are $\sigma(\gamma_0) \approx 6.2$ μb and $\sigma(\gamma_1) \approx 134$ μb [72]. The γ_1 transition also gives rise to 4.44 MeV gammas discharging the first excited state of ^{12}C. The use of high energy resolution HP*Ge* γ-ray spectrometers with an oblique line-of-sight, can provide information on losses of *H*-ions. Modelling shows that the Doppler broadening of the 4.44 MeV γ-line in the spectrum depends on the *H*-ion loss-cone. The calculated Doppler peaks depending on the *H*-ion loss-cone width are presented in figure 14. One can see a sensitivity of the Doppler shape to the loss pitch-angles, $\theta = \arccos(v_{||}/v)$, where $v_{||}$ is the *H*-ion velocity component along the magnetic field. The $^{11}B(p,\gamma)^{12}C$ reaction can be used for *H*-NBI characterisation in both *H*- and *D*-plasmas and the *H*-minority heating of *D*-plasmas.

The inelastic scattering reactions $^{10,11}B(p,p_i\gamma)^{10,11}B$ could be useful for the energy distribution assessment in the case of MeV-energy *H*-ions. The cross-section of the $^{11}B(p,p_1\gamma)^{11}B$ reaction [73] is presented in figure 15. One can see that there is a reaction threshold at $E_p \approx 2.6$ MeV to excite the first level in ^{11}B. As a result, the *H*-ions with $E_H > 2.6$ MeV generate 2.125 MeV gammas. In the case of a very energetic *H*-ion tail, the upper levels can be excited and γ-ray transitions from them will appear in the γ-ray spectrum (see the ^{11}B level scheme in figure 15). In the $^{10}B(p,p_i\gamma)^{10}B$ reaction, the threshold is much lower (≈0.8 MeV) as the first and second levels are at 0.718 and 1.740 MeV (see the ^{10}B level scheme in figure 7(*a*)). For the 1 MeV *H*-NBI characterisation, the 0.718 MeV gammas can be used for monitoring of the beam deposition in the plasma. Note that in the *D*-plasmas, γ-rays of the $^{10}B(p,p_i\gamma)^{10}B$ reaction are in the energy range with a rather high neutron-induced background ($E_\gamma < 3$ MeV), so there are some restrictions for the analysis of discharges with high neutron rates. Nevertheless, gammas generated due to the inelastic scattering $^{10,11}B(p,p_i\gamma)^{10,11}B$ mean that it is possible to characterise *H*-NBI and ICRF heating in *D*-plasmas.

$^{12}C + p$ reactions. In some fusion devices, for example in JT-60SA in its initial experimental stages, carbon will be the main plasma impurity as it was in JET carbon wall operations. Figure 16 demonstrates the γ-ray spectrum recorded during a JET discharge with a very energetic *H*-ion tail. Due to the proton inelastic scattering, $^{12}C(p,p_i\gamma)^{12}C$, the first (4.44 MeV) and second (7.654 MeV) levels were excited (see the ^{12}C level scheme in figure 6). The recorded spectra have allowed assessment of the energetic *H*-ion tail distribution. The cross-section of the $^{12}C(p,p_i\gamma)^{12}C$ reaction [58] is presented in figure 16. One can see that this reaction is very sensitive to MeV protons, which is useful for the ICRF heating characterisation.

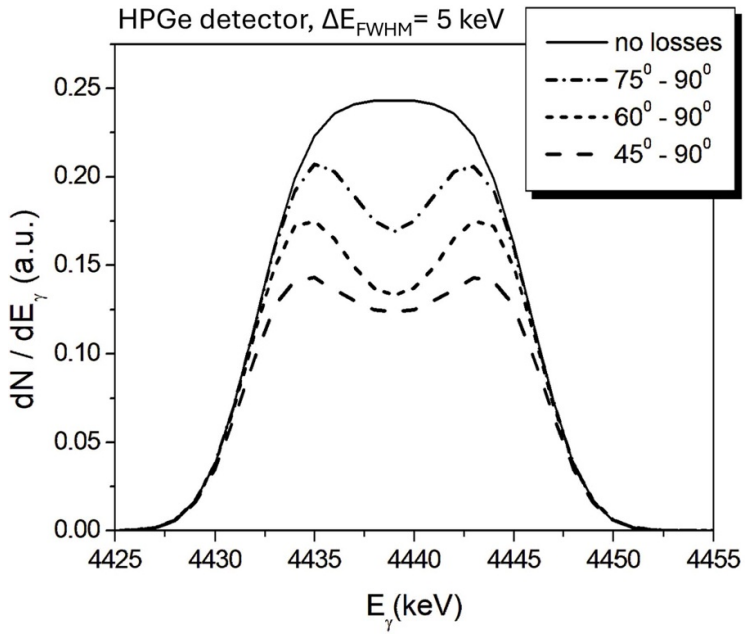

Figure 14. Calculations of the 4.44 MeV γ-ray Doppler broadened peak for different width of the loss-cone, which is characterised by the pitch-angles $\theta = \arccos(v_{||}/v)$.

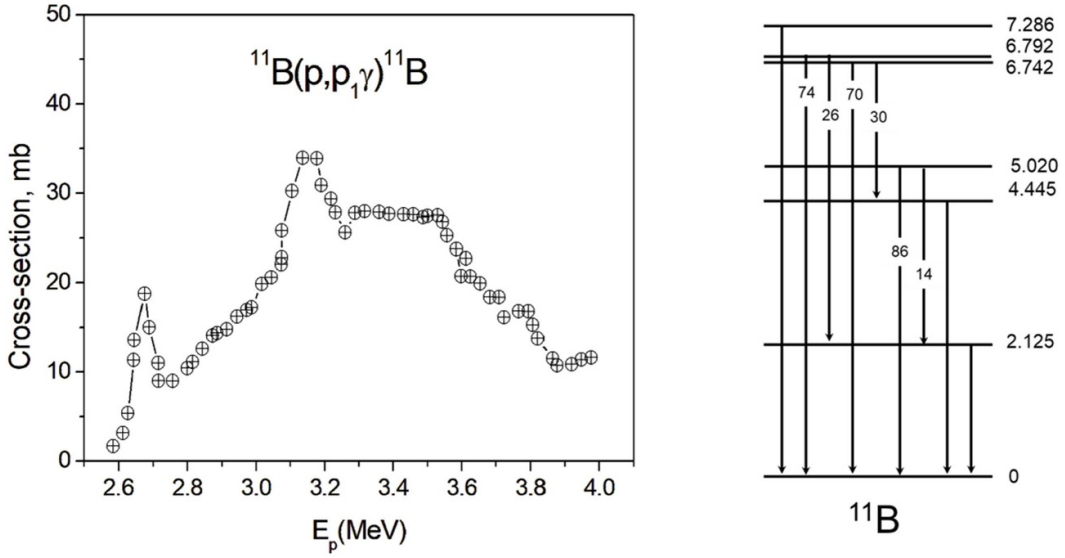

Figure 15. Left—the cross-section of the $^{11}B(p,p_1\gamma)^{11}B$ reaction [73]. Right—scheme of the ^{11}B excited states with γ-ray transitions; branching ratios (%) are shown.

In the radiation capture reaction $^{12}C(p,\gamma)^{13}N$, the reaction has two resonances at $E_{p1} \approx 0.456$ MeV and $E_{p2} \approx 1.700$ MeV with γ_0-transition cross-sections, $\sigma_{p1} \approx 125$ μb ($E_{\gamma 0} = 2.365$ MeV) and $\sigma_{p2} \approx 50$ μb ($E_{\gamma 0} = 3.502$ MeV) [74, 75]. For the *H*-NBI characterisation in *H*-, *D*- and *T*-plasmas it would be especially beneficial to have an additional boron doping of the plasmas. In this case, the use of the $^{12}C(p,\gamma)^{13}N$ reaction (2.365 MeV gammas), together with the boron capture reaction, $^{11}B(p,\gamma)^{12}C$ (4.440 MeV gammas), with the resonance energy $E_p \approx 0.162$ MeV, allows monitoring of the *H*-ion energy distribution during NBI heating.

$^{22}Ne(p,\gamma)^{23}Na$ reaction. This reaction can be useful for diagnosing fast *H*-ions in low-activation plasmas with Ne doping. There are several proton resonances which decay by γ-ray transitions. Figure 17 shows the energy dependence of the relative reactivities of several resonances in the case of the Maxwellian distribution of *H*-ions. The strongest resonances are at 0.639 MeV (≈4 mb) and 1.279 MeV (≈9 mb) energies. This reaction can be exploited in low-activation plasmas only.

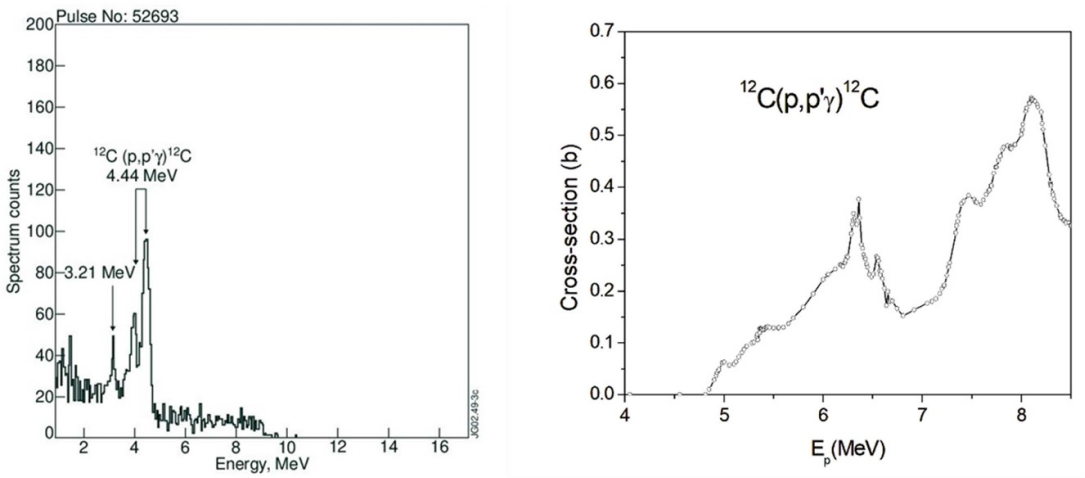

Figure 16. Left—figure 24 showing γ-ray spectrum recorded in 2.8 MA/2.8 T discharge with *H*-minority ICRF heating in a low-density deuterium plasma in JET with a carbon wall. Right—cross-section of the inelastic scattering of protons on carbon [58]. Left figure reproduced from [9].

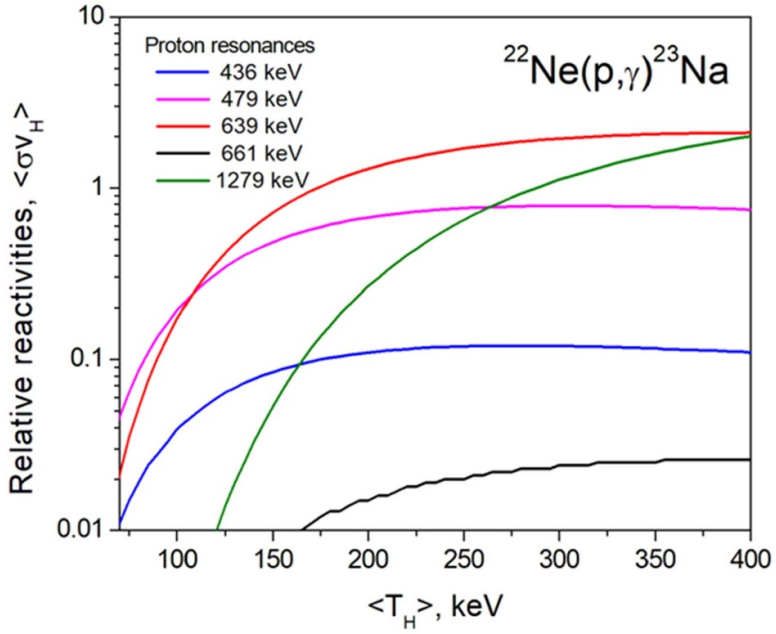

Figure 17. Comparison of reactivities of proton resonances in the $^{22}Ne(p\gamma,)^{23}Na$ reaction [58].

Remarks. Most of the diagnostic reactions in table 2 can be used in low-activation plasmas only. However, the $D(p,\gamma)^3He$ (5.5 MeV γ-rays) and $T(p,\gamma)^4He$ (20 MeV γ-ray) reactions are extremely important for both NBI and ICRF heating scenario developments in deuterium, tritium and *DT*-plasmas.

3.3. Characterisation of heating systems generating energetic D-ions

Generation of fast deuterons is also associated with both NBI and ICRF heating systems. Positive-source NBI systems usually provide fast deuterons with energies up to ∼120 keV, whereas N-NBI systems operate with higher energy deuterons. In JT-60SA and ITER, the N-NBI system will deliver fast deuterons with energies up to 500 keV and 1 MeV, respectively. In this sub-section, a set of selected nuclear reactions, proposed in table 3, for γ-ray diagnosis of energetic *D*-ions in plasmas is discussed.

In JET, the main source of energetic *D*-ions in the MeV-energy range was ICRF heating, i.e. harmonics and 3-ion ICRH schemes [29]. The energetic *D*-ion tail was characterised using γ-rays from $T(d,\gamma)^5Li$, $^3He(d,\gamma)^5Li$, $^9Be(d,n\gamma)^{10}B$, $^9Be(d,p\gamma)^{10}Be$ and $^{12}C(d,p\gamma)^{13}C$ reactions [9]. In the non-beryllium machines, the energetic *D*-beams can be characterised with γ-ray measurements in *H*-, *D*-, *T*-, *He*- and D^3He-plasmas.

Table 3. Diagnostic nuclear reactions for characterisation of energetic deuterons.

Reaction	Energy of reaction, Q (MeV)	Energy of gammas, E_γ (MeV)	Reaction application comments
$H(d,\gamma)^3He$	5.49	5.5	H-plasma; $E_{NBI} > 0.4$ MeV
$D(d,\gamma)^4He$	23.85	24	D-, DT-plasma; $\sigma \sim 0.02$ μb @ 1 MeV
$T(d,\gamma)^5He$	16.79	17	T-plasma; NBI performance, $E_{Res} \approx 0.11$ MeV
$^3He(d,\gamma)^5Li$	16.66	17	D^3He—plasmas; NBI $E_{Res} \approx 0.45$ MeV
$^4He(d,\gamma)^6Li$	1.474	2.186	He-plasmas, $E_d > 1.1$ MeV
$^6Li(d,n\gamma)^7Be$	3.381	0.429	H-, He-plasmas
$^6Li(d,p\gamma)^7Li$	5.026	0.478	
$^{10}B(d,n\gamma)^{11}C$	6.4648	2.0, 4.319, 4.80 etc	B-doping
$^{10}B(d,p\gamma)^{11}B$	9.2296	2.12, 4.445, 5.02 etc	
$^{11}B(d,n\gamma)^{12}C$	13.732	4.440, 3.21 & 9.64	
$^{11}B(d,\alpha\gamma)^9Be$	8.031	1.68, 2.43, 3.05, 6.38	
$^{12}C(d,p\gamma)^{13}C$	2.722	3.09	C-impurity; $E_D > 0.43$ keV

Deuteron radiation capture reactions. In the H-plasma, 5.5 MeV γ-rays from the $H(d,\gamma)^3He$ reaction can be used for commissioning and studying D-NBI heating with beams $E_{NBI} > 0.4$ MeV. In the case of injection of the 1 MeV D-beams in D-plasmas, an effective core ion-temperature can be inferred with a $D(d,\gamma)^4He$ capture reaction, which produces 24 MeV gammas. Indeed, the cross-section of this reaction reaches ≈0.02 μb at $E_D = 1$ MeV [58], so the 24 MeV γ-ray emissivity could be measurable in discharges with energetic NBI ions, e.g. in ITER. A negligible background in this γ-ray energy range allows for a credible analysis of the broadening of the 24 MeV peak that is related to the deuteron distribution function.

In deuterium plasmas with some ^3He doping, the D-NBI performance can be monitored by measuring the 17 MeV γ-ray emission from the $^3He(d,\gamma)^5Li$ reaction as it was routinely done on JET. It is important to note that the reaction cross-section has a broad resonance at $E_D \approx 0.45$ MeV. Since the $^3He(d,p)^4He$ reaction gives rise to 3.6 MeV α-particles, this type of experiment could also be used for tests of the α-particle diagnostics prior to DT-plasma studies.

Furthermore, it is very important to set up an optimal transition from L- to H-mode [76]. Before full-scale burning plasma experiments in the established H-mode, final characterisation of the D-NBI could be done in full T-plasmas. A straightforward method of L–H transition monitoring could be measurements of 17 MeV γ-rays from the $T(d,\gamma)^5He$ reaction.

In exotic He-plasma experiments, energetic D-ions with $E_D > 1.1$ MeV can excite the first level of ^6Li due to the capture reaction $^4He(d,\gamma)^6Li$ producing 2.186 MeV gammas. The D-ions below 1 MeV will give rise to the radiation capture γ-ray spectrum, which can be defined as $E_\gamma \approx Q + 2E_d/3$.

$^6Li + d$ reactions. Doping the plasma with lithium can be used for the D-NBI characterisation in H- and He-plasmas. In this case, the $^6Li(d,n\gamma)^7Be$ and $^6Li(d,p\gamma)^7Li$ reactions produce γ-rays due to discharging the first excited states with energies 0.429 MeV ($^7Be^*$) and 0.478 MeV ($^7Li^*$). The available cross-sections shown in figure 18 increase monotonically, so these cross-sections data could be easily extrapolated to a required energy range.

$^{10,11}B + d$ reactions. These reactions are the most demanding because boronisation of the reactor wall is suggested for several machines including ITER. Among the available boron reactions, the $^{11}B(d,n\gamma)^{12}C$ and $^{11}B(d,\alpha\gamma)^9Be$ reactions are most practical since they have large cross-sections (figure 19) and an 80% abundance of the ^{11}B isotope. 1 MeV NBI deuterons can excite the ^{12}C levels up to 15.6 MeV (see the ^{12}C level scheme in figure 6) and the ^9Be levels up to 8.9 MeV (see figure 20(*a*)). Gamma-ray decays of the ^{12}C excited states 4.440, 7.654 and 9.641 MeV give rise to the strongest γ-ray emission. Also, the $^{11}B(d,\alpha\gamma)^9Be$ reaction can be useful for the D-beam characterisation; however the expected γ-ray emissivity from this reaction is much less than from $^{11}B(d,n\gamma)^{12}$C. The γ-ray decay of the ^9Be levels 1.684, 2.429 and 3.049 MeV could be measured, however the dominant decay of the 2.429 MeV state is $^5He_{g.s.} + \alpha$, while the 3.049 and 4.704 MeV states decay with neutrons, i.e. $^8Be_{g.s.} + n$. These reactions could also be used for the characterisation of NBI heating with $E_D < 0.5$ MeV. The reaction cross-sections

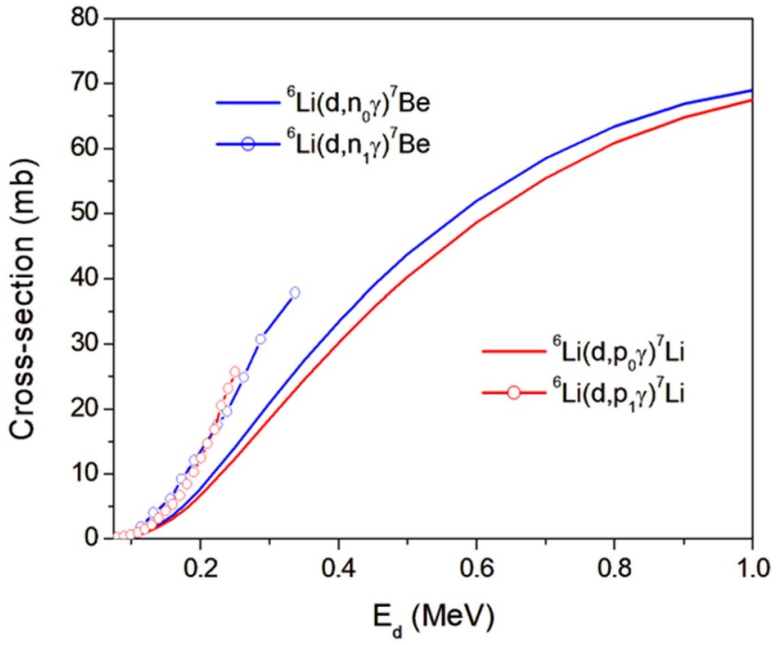

Figure 18. Cross-sections of the $^{6}Li(d,n_i\gamma)^{7}Be$ and $^{6}Li(d,p_i\gamma)^{7}Li$ reactions [58] related to the ground (i = 0) and first excited states (i = 1).

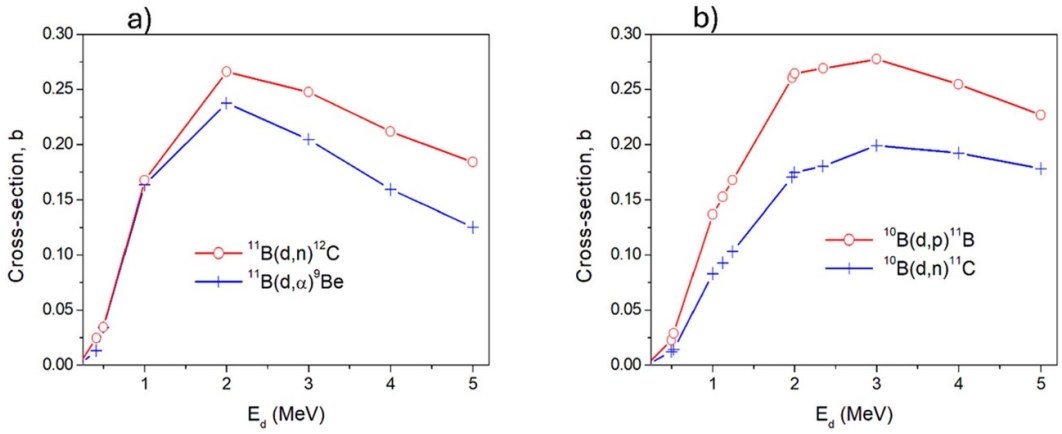

Figure 19. Evaluated total nuclear reaction cross-sections [58]. (*a*) $^{11}B(d,n\gamma)^{12}C$ and $^{11}B(d,\alpha)^{9}Be$ reactions. (*b*) $^{10}B(d,p)^{11}B$ and $^{10}B(d,n)^{11}C$ reactions.

presented in figure 21 are obtained by measuring n_0- and n_1-neutrons [77] and α_0- and α_1-alphas [78] in the low-energy deuteron experiments.

According to the available total reaction cross-section data shown in figure 19, the $^{10}B(d,n\gamma)^{11}C$ (see the scheme of ^{11}C excited states with γ-ray transitions in figure 20(*b*)) and $^{10}B(d,p\gamma)^{11}B$ reactions can be used for the NBI characterisation; however, the ^{10}B isotope has 20% abundance, so in the boron-doped plasma, its concentration would be four times less than ^{11}B. Figure 22 shows the partial $^{10}B(d,p)^{11}B$ reaction cross-sections for the low-energy [78] and MeV-energy deuterons, which are related to the excitation of the first three levels in ^{11}B (see the scheme of ^{11}B excited states with γ-ray transitions in figure 15). Note that the γ-ray emissions 2.12, 4.445 and 5.02 MeV due to the decay of these levels dominate.

$^{12}C(d,p\gamma)^{13}C$ reaction. Since this reaction goes with Q = 2.722 MeV, only energetic deuterons can excite the first ^{13}C level, 3.089 MeV (see the scheme of ^{13}C excited states with γ-ray transitions in figure 23(*a*)). This is an important reaction for the *D*-beam characterisation as the energy threshold for excitation of the 3.089 MeV level is 0.43 MeV. Hence, deuterons with energies exceeding this threshold give rise to 3.089 MeV γ-ray emission. The cross-section of the excitation of this level is presented in figure 23(*b*).

One can conclude that using a combination of nuclear reactions for γ-ray diagnosis of energetic *D*-ions listed in table 3 could provide valuable information on the characterisation of *D*-NBI heating in plasmas.

Remarks. In devices with boronisation, $^{10,11}B + d$ reactions could be very informative for the fast *D*-ions characterisation

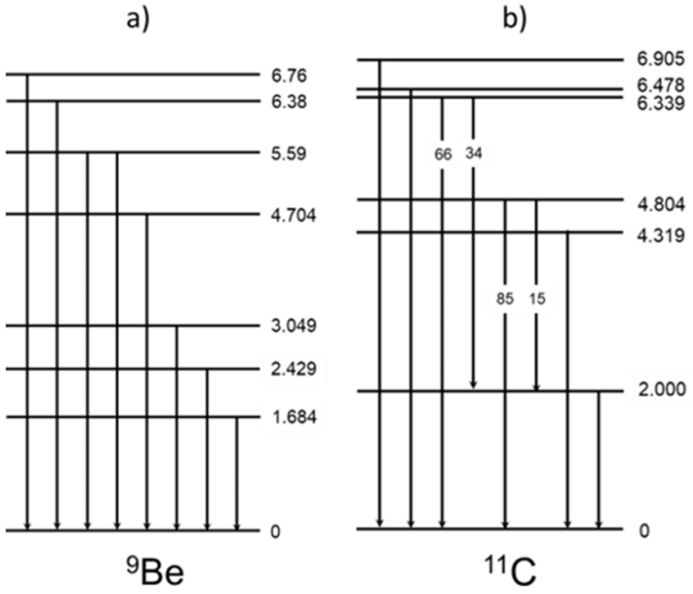

Figure 20. ^{9}Be and ^{11}C level schemes with γ-ray transitions and branching ratios (%) [58].

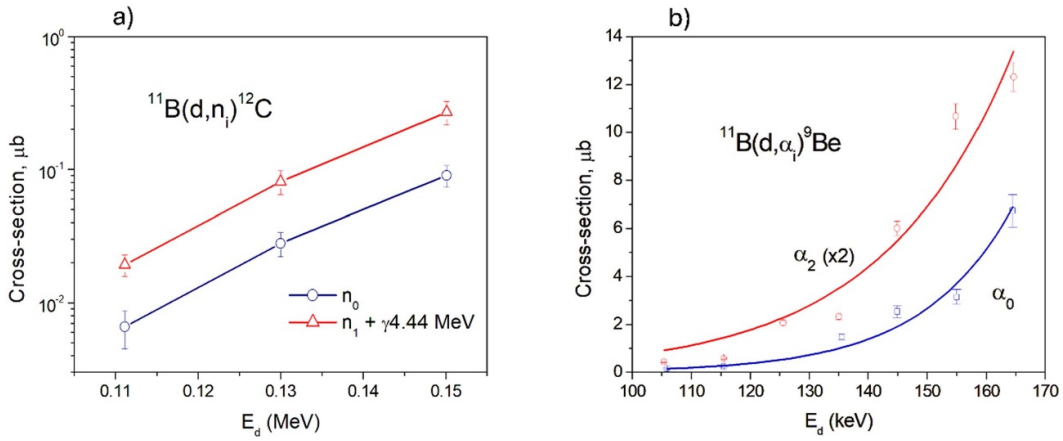

Figure 21. Experimental cross-sections related to the population of excited states at low energies of deuterons. (*a*) $^{10}B(d,n_i)^{11}C$ reaction [77]. (*b*) $^{11}B(d,\alpha_i)^{9}Be$ reaction ^{9}Be [78].

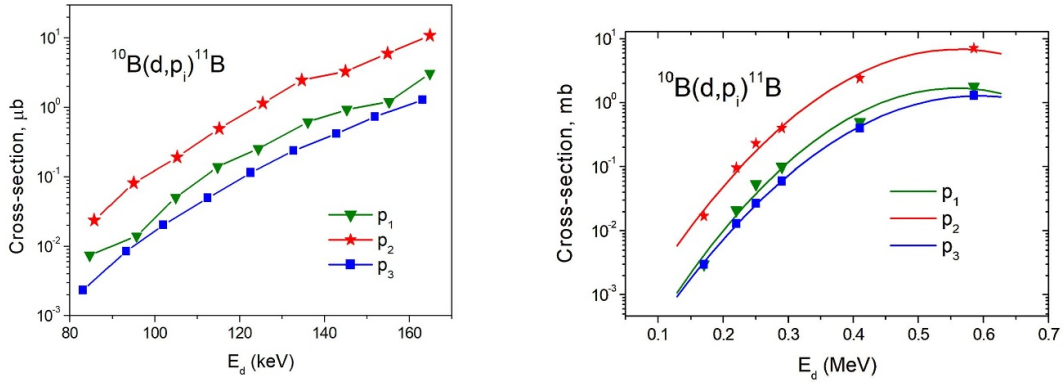

Figure 22. Experimental cross-sections of the $^{10}B(d,p)^{11}B$ reaction related to the population of the first three excited states of ^{11}B. Left—low energy deuteron data [78]. Right—MeV range deuteron data [58] with the fitted curves.

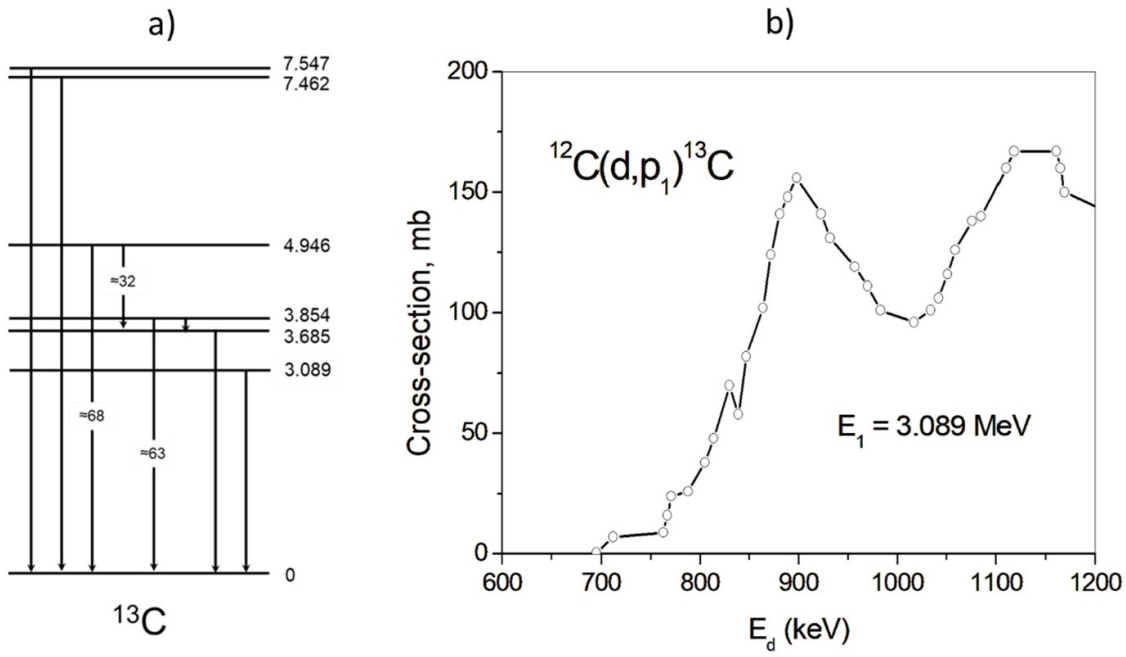

Figure 23. (*a*) ^{13}C level scheme with γ-ray transitions and branching ratios (%) [58]. (*b*) Experimental cross-section of the $^{12}C(d,p)^{13}C$ reaction [79] related to the population of the first excited state of ^{13}C.

in high performance experiments; in machines with carbon as the main impurity (e.g. JT-60SA), the $^{12}C(d,p\gamma)^{14}N$ reaction, which was widely used on JET, would be a perfect alternative.

4. Optimisation of *D*- and *DT*-plasma scenarios

Generation of the 1 MeV tritons in the fusion reaction *D(D,p)T* leads to their 'burnup' during slowing down, giving rise to 14 MeV neutrons from the $D(t,n)^4He$ reaction and 17 MeV gammas from its branch, $D(t,\gamma)^5He$. There is a maximum of these emissions at the resonance energy $E_T \approx 160$ keV. As a rule, 14 MeV neutron monitors/spectrometers have been used to study the confinement and slowing-down of fast tritons in deuterium plasmas [80–84]. In JET, 17 MeV γ-rays and prompt triton losses were also measured for a comprehensive study of the ICRF heating performance [85]. Monitoring of the 17 MeV gammas were routine measurements. An example of the γ-ray spectrum, which is recorded in a high-performance JET deuterium discharge by the *BGO*-scintillator detector, is shown in figure 24. The gammas related to the $D(t,\gamma)^5He$ reaction are measured in the range $E_\gamma \approx 12$–17 MeV. The neutron-induced γ-ray background emission is rather intense in the energy range below ∼10 MeV deuterium plasmas. A finite slowing-down time of *DD*-tritons from the birth energy to the maximum of the *D–T* fusion reaction leads to a difference between the *DD*-neutron and 17 MeV γ-ray rate waveforms. One can see in figure 24 that the 17 MeV γ-rays are delayed relative to the neutron rate. As a rule, analysis of *DD*- and *DT*-neutron rates is used to infer the triton slowing-down time. However, monitoring of the 17 MeV γ-rays is preferable because the 14 MeV neutron measurements and analysis are rather complicated by reason of a low detection efficiency. In addition, the energetic MeV-tritons generate γ-rays from selected nuclear reactions in table 4, so the monitoring of these γ-rays can provide a figure of merit of the heating performance and information on the triton source distribution function.

$^{11}B + t$ and $^{12}C + t$ reactions. In plasmas with boron impurity, the $^{11}B(t,n\gamma)^{13}C$ and $^{11}B(t,2n\gamma)^{12}C$ reactions can be used for analysis of the triton energy distribution. In figure 25, one can see that the $^{11}B(t,2n\gamma)^{12}C$ cross-section is highest. According to the ^{12}C decay scheme (see figure 6), 1 MeV *DD*-tritons can excite the first two levels, hence the 4.44 MeV and 3.21 MeV γ-rays could be in the spectrum. However, tritons with energies $E_t < 0.24$ MeV can excite the 4.44 MeV level only, so 3.21 MeV gammas are not generated. In this case, the ratio of the 4.44 MeV and 3.21 MeV γ-ray peaks depends on the triton energy distribution. Since the $^{11}B(t,n\gamma)^{13}C$ reaction has Q = 12.421 MeV, high-energy levels of ^{13}C up to 13 MeV are excited (see the level scheme of ^{13}C in figure 23(*a*)). The most intensive γ-rays, 3.09 MeV, 3.68 MeV and 3.85 MeV will be in the spectrum, though gammas related to decays of the high-energy levels, 4.946 MeV, 7.462 MeV and 7.547 MeV, could appear as well.

The $^{12}C(t,n\gamma)^{14}N$ reaction could be useful in the case of a small concentration of carbon in the plasma. The cross-section of the reaction (see figure 25) is sufficient for the diagnosis of MeV tritons. Decays of the first two excited states in ^{14}N (see the level scheme in figure 5) provide a strong emission of 2.312 MeV and 1.635 MeV γ-rays. The energy distribution of the *DD*-tritons at birth depends on an effective temperature

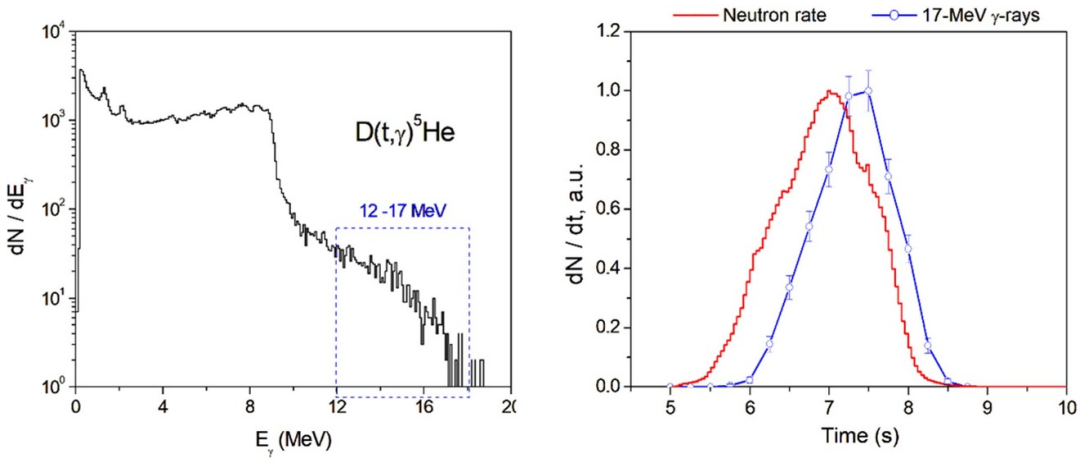

Figure 24. Gamma-ray spectrum recorded in JET deuterium discharge #40554 (left); waveforms of total neutron rate and γ-ray emission rate of the $D(t,\gamma)^5He$ reaction in the energy range 12–17 MeV (blue dash-box marked in left figure).

Table 4. Diagnostic nuclear reactions for characterisation of energetic tritons.

Reaction	Energy of reaction, Q (MeV)	Energy of gammas, E_γ (MeV)	Reaction application comments
$D(t,\gamma)^5He$	16.79	17	*D*-plasma; triton burnup monitoring
$^{11}B(t,n\gamma)^{13}C$	12.421	3.09, 3.68, 3.85 etc	*D*-plasma, *B* doping; triton burnup monitoring
$^{11}B(t,2n\gamma)^{12}C$	7.475	4.44 & 3.21	
$^{12}C(t,n\gamma)^{14}N$	4.015	2.312 & 1.635	*D*-plasma, *C* impurity; triton burnup monitoring
$D(T,\gamma)^5He$	16.79	17	*DT*-plasma: α-particle rate
$T(p\gamma)^4He$	19.814	20	*DT*-plasma: *DD*-protons rate, core temperature & fuel ratio

of deuterons. Due to an auxiliary heating of the plasma, the *DD*-tritons could have energy exceeding 1 MeV. Tritons with $E_t > 1.13$ MeV can excite the level at 4.915 MeV, and triton energy $E_t \approx 1.36$ MeV is a threshold for excitation of the 5.108 MeV level. Thus, measurements of γ-ray emission due to the decay of these levels can provide information on the *DD*-triton source in ICRF heated plasmas.

$D(T,\gamma)^5He$ & $T(p,\gamma)^4He$ reactions. JET experiments with *D–T* plasmas already showed that the rate of 17 MeV γ-rays from the $D(T,\gamma)^5He$ reaction can be a figure of merit of the heating performance in addition to the 14 MeV neutron rate [12]. In addition, as previously discussed, measurements of 20 MeV γ-rays from the $T(p,\gamma)^4He$ reaction can be used for the *H*-minority heating characterisation. In *D–T* plasma, simultaneous measurements of the 20 MeV and 17 MeV gammas are rather useful for the development of high-performance scenarios. Indeed, the *D–T* fusion rate depends on the effective *H*-ion temperature due to ICRF heating, which can be inferred by measuring of the 20 MeV peak broadening. As an example of the use of this plasma optimisation tool, a comparison of two γ-ray spectra recorded in JET *D–T* discharges at the central toroidal field $B_0 = 3.3$ T and plasma current $I_p = 2.0$ MA, i.e. during the *H*-minority and second harmonic *T* ICRF heating, is presented in figure 26.

It is important to note that in burning plasmas, 20 MeV γ-rays are generated by *DD*-protons. As shown in [86], simultaneous measurements of $D(T,\gamma)^5He$ and $T(p,\gamma)^4He$ reactions can monitor the fuel ratio, n_D/n_T, in the plasma core; the 20 MeV γ-rays from the $T(p,\gamma)^4He$ reaction give an effective electron temperature (T_e). Indeed, this is a unique diagnostic tool for reactor plasmas.

Remarks. The 17 MeV gammas of the $D(t,\gamma)^5He$ reaction and the $^{11}B(t,2n\gamma)^{12}C$ reaction γ-rays could be a powerful diagnostic tool for the triton burnup monitoring in high-performance deuterium plasmas with boronisation. Measurements of the $D(T,\gamma)^5He$ and $T(p,\gamma)^4He$ reactions allow us to tune the *D–T* plasma scenarios and monitor important parameters (the fuel ration and T_e) in the burning plasma.

5. Alpha-particle studies

There are several nuclear fusion reactions which give rise to α-particles: $D(T,n)^4He$, $D(^3He,p)^4He$, $T(T,2n)^4He$, and

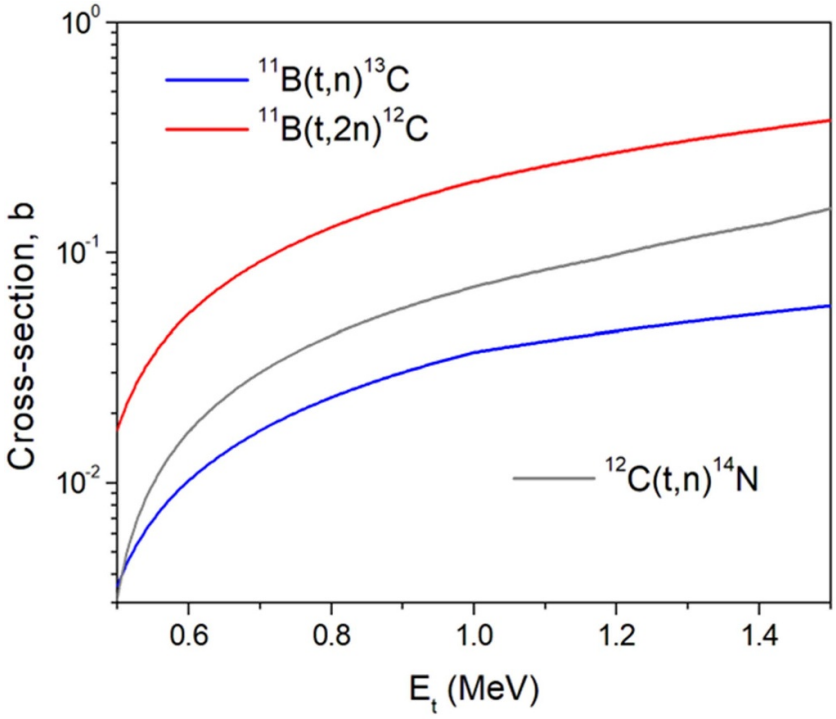

Figure 25. Evaluated total nuclear reaction cross-sections of $^{11}B(t,n)^{13}C$, $^{11}B(t,2n)^{12}C$ and $^{12}C(t,n)^{14}N$ reactions [58].

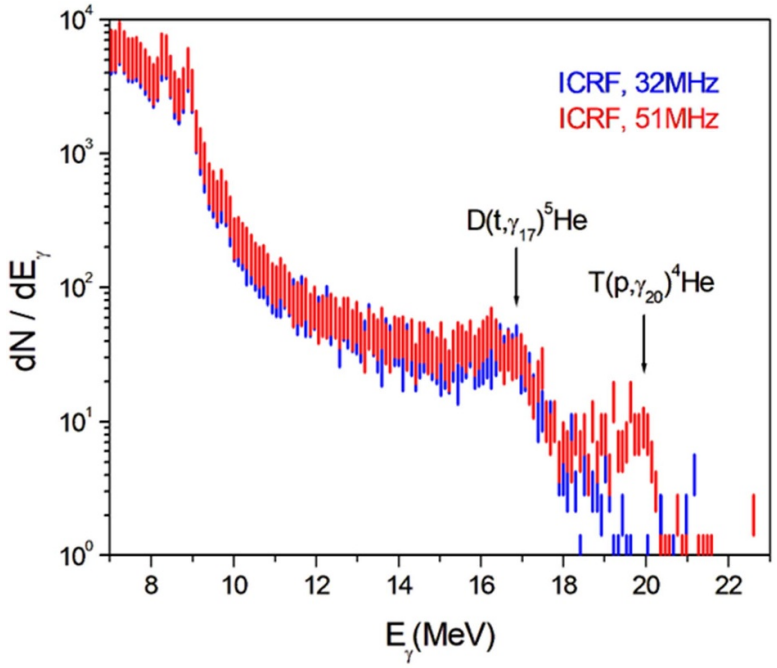

Figure 26. Gamma-ray spectra recoded in JET *D–T* discharges at 3.3 T/2.0 MA: red-lines—*H*-minority (51 MHz); blue-lines—second harmonic *T*-heating (32 MHz).

$^{11}B(p,2\alpha)^4He$. In the first two reactions, alphas have nearly the same birth-energy, ≈3.5 MeV and ≈3.6 MeV, respectively. The birth-energy spectra of the last two reactions have continuous features due to the kinematics of three outgoing particles in the final state. Tritium-beam experiments [87] have found that the energies of the *T–T* α-particles are below ≈3.8 MeV. Measurements of the first-orbit α-particle losses in JET tritium plasmas with 110 keV *T*-NBI heating showed a broad loss-peak at $E_\alpha \approx 4$ MeV [12]. The well-known 3-alphas ^{11}Bp-reaction (Q = 8.682 MeV) has a strong resonance at $E_H \approx 0.675$ MeV with a total cross-section ≈1.4 b [71]. The ^{11}Bp-reaction experiments revealed that at the resonance there is a broad peak in the α-particle spectrum at $E_\alpha \approx 4.3$ MeV. As such, the α-particle studies in *D–T, D–*^{3}*He, T–T* and ^{11}B*–H*

fusion plasmas need to be carried out in a wide range of α-particle energies. Several γ-ray diagnostic reactions are selected (see table 5) for α-particle studies in plasmas with different levels of the neutron-induced γ-ray background.

D–T plasma. In plasmas with boron impurities, γ-ray measurements of the α-particles can be studied with $^{10}B(\alpha,n\gamma)^{13}N$ and $^{10}B(\alpha,p\gamma)^{13}C$ reactions. The $^{10}B(\alpha,p\gamma)^{13}C$ reaction was proposed as an alternative to the $^{9}Be(\alpha,n\gamma)^{12}C$ diagnostic reaction for ITER in the past [88]. Indeed, alpha-particles with the energy $E_\alpha > 1$ MeV give rise to γ-rays which are discharging the first three excited states of ^{13}C shown in figure 23(*a*). Excitation functions of these states, 3.089 MeV, 3.684 MeV and 3.854 MeV, were obtained from the measured γ-ray angular distributions in the α-particle energy range 1.25–4.2 MeV [89]. The low-energy cross-sections of the $^{10}B(\alpha,p\gamma)^{13}C$ reaction in the range 2.5 MeV $> E_\alpha >$ 0.57 MeV were measured in recent experiments [90]. Comparison of both data sets in the overlapped energy range shows a good agreement (see figure 27).

Note that there are some benefits of using the $^{10}B(\alpha,p\gamma)^{13}C$ reaction instead of the $^{9}Be(\alpha,n\gamma)^{12}C$ one. The boron reaction can provide information on alphas in the energy range $E_\alpha > 1$ MeV, while *D–T* α-particles with $E_\alpha > 1.7$ MeV can be studied with the $^{9}Be(\alpha,n\gamma)^{12}C$ reaction. Furthermore, information on α-particles, which could be obtained from γ-rays by means of three excited levels in the $^{10}B(\alpha,p\gamma)^{13}C$ reaction, is more convincing than data from two excited levels in the $^{9}Be(\alpha,n\gamma)^{12}C$ reaction. However, the drawback of the boron reaction is the lower cross-section, i.e. the rate of 3.854 MeV gammas by a factor of 2–2.5 less than the 4.44 MeV emission in the $^{9}Be(\alpha,n\gamma)^{12}C$ reaction. In addition, the ^{10}B isotope abundance is ≈20%, though the vessel boronisation with the ^{10}B isotope would not be expensive. Nevertheless, γ-ray diagnostics of confined α-particles with $E_\alpha > 1$ MeV in fusion devices with boron plasma impurity using the $^{10}B(\alpha,p\gamma)^{13}C$ reaction are promising and could be experimentally tested and validated in low-activation plasma devices, as was conducted in the case of the $^{9}Be(\alpha,n\gamma)^{12}C$ reaction on JET [9, 32]. The yield of the 3.089 MeV, 3.684 MeV and 3.854 MeV γ-rays can be measured by scintillation detectors as well as HP*Ge* detectors, which provide high-resolution γ-ray spectrometry. In the case of the HP*Ge* detector, an analysis of the Doppler broadened γ-ray peaks could deliver information on the energy distribution of α-particles in the plasma (see the use of this method on JET [17]).

An advanced technique to measure α-particles escaping the plasma and striking the wall, known as γ-ray monitor of the lost α-particles (GRAM), has been proposed for ITER in [91]. It is a rather simple and robust method, which does not require access to the reactor vacuum vessel. The lost α-particle rate can be measured by a γ-ray spectrometer viewing the boronated wall or a specially-installed target with a thin boron layer. Furthermore, in low-activation plasmas, the use of a collimated HP*Ge* spectrometer could allow measurements of the pitch-angle distribution of lost α-particles, as proposed in [89]. Indeed, since the 3.089 MeV and 3.684 MeV excited states in $^{13}C^*$ have got ≈1 fs lifetimes, the γ-line Doppler shape analysis is available. Hence, the velocity space of the lost α-particles can be inferred.

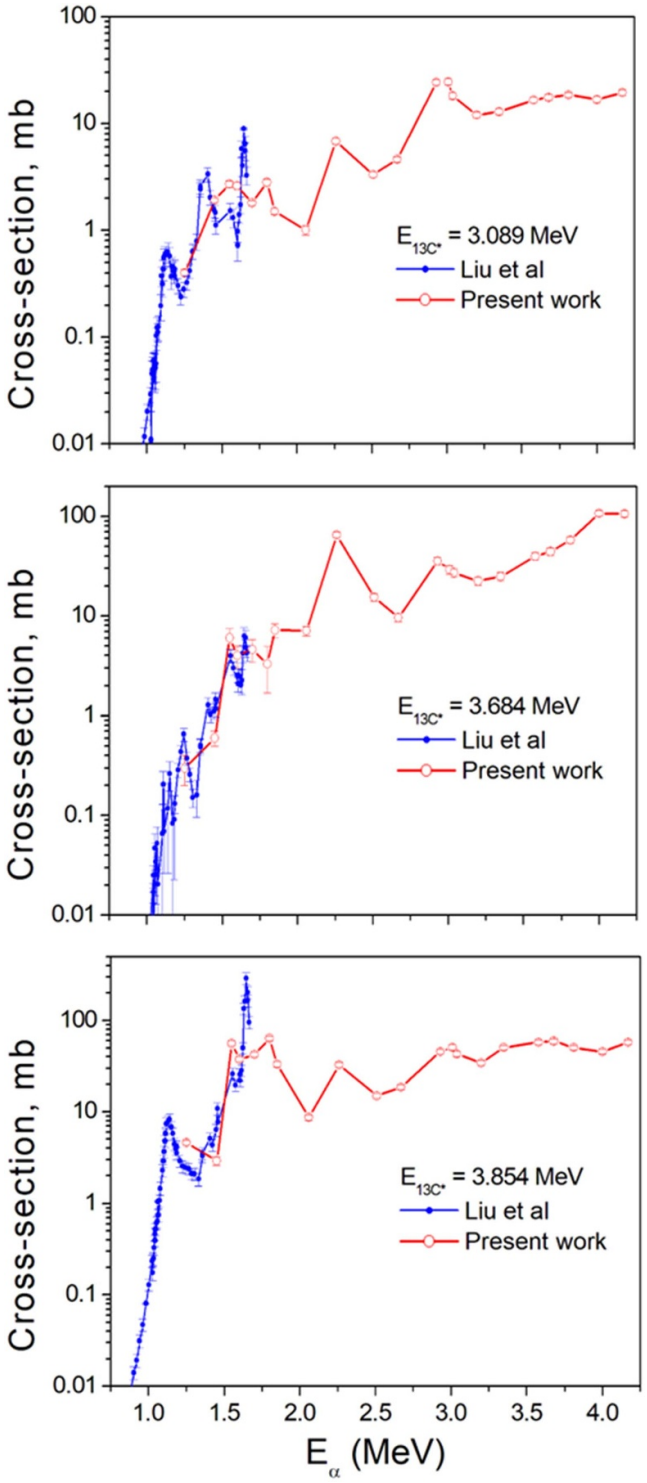

Figure 27. Excitation functions of the first three states in the $^{10}B(\alpha,p\gamma)^{13}C$ reaction obtained in [89, 90]. Reprinted from [20], copyright (2025), with permission from Elsevier.

The $^{10}B(\alpha,n\gamma)^{13}N$ reaction (Q = 1.059 MeV) gives rise to 2.368 MeV γ-rays if the α-particle energy exceeds ≈1.8 MeV.

Table 5. Diagnostic nuclear reactions for α-particle studies.

Reaction	Energy of reaction, Q (MeV)	Energy of gammas, E_γ (MeV)	Reaction application comments
$^{6}Li(\alpha,\gamma)^{10}B$	4.461	γ_0, γ_1, γ_2, γ_3 and 0.718, 1.740, 2.154	Low-activation plasmas; $E_{Res} \approx$ 1.17, 2.43, 4.02 MeV
$^{7}Li(\alpha,\gamma)^{11}B$	8.66	γ_0, γ_2 and 4.44	$E_{Res} \approx$ 0.402, 0.815 & 0.954 MeV
$^{10}B(\alpha,p\gamma)^{13}C$	4.061	3.09, 3.68 & 3.85	*D–T* plasma; $E_\alpha > 1$ MeV
$^{10}B(\alpha,n\gamma)^{13}N$	1.059	2.368	*D–T* plasma; $E_\alpha > 1.8$ MeV
		3.50	$E_\alpha > 3.4$ MeV
$^{11}B(\alpha,n\gamma)^{14}N$	0.158	2.313	Low-activation plasmas; $E_\alpha > 3$ MeV
		1.635	$E_\alpha > 4.6$ MeV
$^{20}Ne(\alpha,\alpha'\gamma)^{20}Ne$	—	1.634	Low-activation plasmas
$^{22}Ne(\alpha,\alpha'\gamma)^{22}Ne$	—	1.275	
$^{20}Ne(\alpha,\gamma)^{24}Mg$	9.316	γ_0, γ_1	Low-activation plasmas
$^{22}Ne(\alpha,\gamma)^{26}Mg$	10.615	γ_0, γ_1	
$^{22}Ne(\alpha,n\gamma)^{25}Mg$	−0.478	$E_\gamma < 3.4$ MeV	Low-activation plasmas; $E_\alpha > 1.4$ MeV

These gammas could therefore be used for the identification of energetic confined alphas in low-activation plasmas, as in *D–T* plasmas these gammas are in the energy range of a high neutron-induced background. The ^{13}N state at 3.502 MeV (see figure 28(*a*)) is excited by alphas with energy higher than $E_\alpha \approx 3.4$ MeV, so 3.50 MeV gammas can be used for α-particle studies in the *D–T* phase as well. Note that the 3.50 MeV gammas could cause a complication for the analysis of the γ-rays from the $^{10}B(\alpha,p\gamma)^{13}C$ reaction because of a specific γ-ray response function of solid-state detectors. Gamma-rays with energy $E_\gamma > 2m_ec^2$ appear in the γ-ray spectrum as three peaks: full energy at E_γ, single escape at $E_\gamma - m_ec^2$ and double escape at $E_\gamma - 2m_ec^2$. As such, when analysing γ-ray emission from the $^{10}B(\alpha,p\gamma)^{13}C$ reaction, this should be taken into account. This is not the case when using measurements for high-resolution Ge-detectors.

Low-activation plasmas. In JET, α-particles were studied using several ICRF plasma heating schemes, i.e. the *He*-ion beam acceleration by the third harmonic [12] in *He*-plasmas and *D*-ion beam acceleration in D^3He-plasmas and the 3-ion ICRH scheme with D-NBI ion acceleration in the D^3He-plasma, generating 3.6 MeV fusion alphas [20]. However, there is an opportunity to study energetic α-particles before *D–T* experiments measuring MeV α-particles from the $^{11}B(p,2\alpha)^4He$ and $^3He(D,p)^4He$ fusion reactions. For this purpose, an appropriate concentration of boron in plasmas is needed both for the α-particle production and their diagnosis. According to the cross-section data of the p–^{11}B and D–^3He fusion reactions, NBI heating with beam-ion energies $E_{NBI} > 0.4$ MeV is required to generate a suitable α-particle source in *H*- and D^3He-plasmas. In fusion devices with ICRF capabilities, D–^3He experiments could also explore α-particle generation using ^3He-minority heating, third harmonic *D*-ion acceleration [92] or the 3-ion D–(D_{NBI})–^3He scheme [93]. As scientific exploitation of the JT-60SA tokamak has already started, fast α-particle studies in the *H*-plasmas with hydrogen N-NBI and, in the low-activation D–^3He plasmas with deuterium N-NBI heating are proposed [94, 95]. A boron dropper as well as neutron and γ-ray spectrometers are needed to realise these studies. Note that the first successful p–^{11}B experiments—using N-NBI heating [96], and H-minority beam acceleration [97]—have been carried out on the LHD with a boron dropper; lost α-particles from the $^{11}B(p,2\alpha)^4He$ reaction were detected.

In low-activation plasmas, boron reactions $^{11}B(\alpha,n\gamma)^{14}N$, $^{10}B(\alpha,n\gamma)^{13}N$ and $^{10}B(\alpha,p\gamma)^{13}C$, which were discussed above, can be used for the diagnosis of MeV α-particles both with γ-ray and neutron diagnostics. Indeed, the partial cross-sections of the $^{10}B(\alpha,n\gamma)^{13}N$ reaction presented in figure 28(*b*) shows that α-particles with energies $E_\alpha > 1$ MeV generate energetic neutrons, so in the low-activation plasma experiments, this fact is very important. One needs to note that neutrons, n_0, de-exciting the compound nuclei $^{14}N^*$ to the ground state of ^{13}N, are most energetic, e.g. at $E_\alpha = 1.5$ MeV neutrons have the energy $E_n \approx 2$ MeV. Neutrons, n_1, n_2 and n_3, feeding the excited states of $^{13}N^*$ are much less energetic. Figure 29(*a*) shows total neutron spectra from the $^{10}B(\alpha,n\gamma)^{13}N$ reaction that are expected in the different α-particle energy distributions presented in figure 29(*b*). One can see that the neutron yield is rather sensitive to the energy distribution of α-particles. Note that in D^3He-plasmas, only n_0-neutrons can be used for α-particle studies since the 2.5 MeV neutron emission due to the $D(D,n)^3He$ reaction is relatively strong and could be an obstacle for the α-particle analysis. However, in *H*-plasmas, measuring MeV α-particles from the $^{11}B(p,2\alpha)^4He$ reaction, the whole neutron spectrum from the $^{10}B(\alpha,n\gamma)^{13}N$ reaction could be available for the analysis.

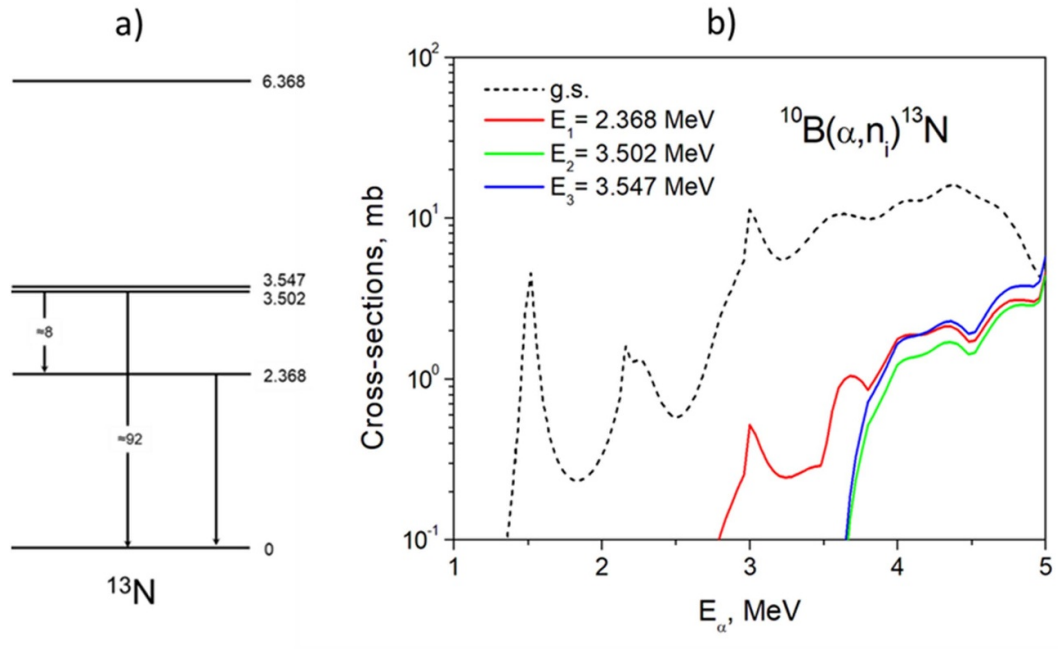

Figure 28. (*a*) ^{13}N level scheme with γ-ray transitions and (*b*) partial cross-sections of the $^{10}B(\alpha,n)^{13}N$ reaction [58].

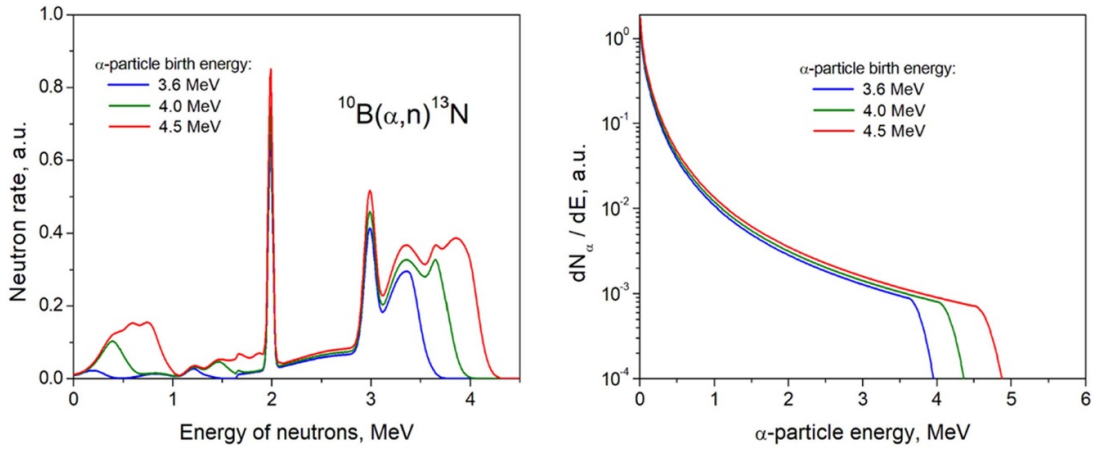

Figure 29. (*a*) Calculated energy spectra of neutrons from the $^{10}B(\alpha,n\gamma)^{13}N$ based on the available reaction cross-sections [58] (see figure 28(*b*)) and energy distribution functions of confined α-particles (*b*), which are born at 3.6, 4.0 and 4.5 MeV.

As to the $^{11}B(\alpha,n\gamma)^{14}N$ reaction, it has a rather small energy yield, Q = 0.158 MeV. Therefore, the reaction gives rise to 2.313 MeV γ-rays by α-particles with energy $E_\alpha > 3$ MeV (see the ^{14}N level scheme in figure 5); more energetic alphas, i.e. $E_\alpha > 4.6$ MeV, also generate 1.635 MeV γ-rays. Since the evaluated total cross-section for the γ-ray production [58] exceeds 100 mb in the range $E_\alpha > 3$ MeV (figure 30), γ-ray detection could be feasible for energetic α-particle studies. In addition, measurements of neutrons would be useful in *H*-plasmas, but complete cross-section data of this reaction are needed.

The $^{6,7}Li(\alpha,\gamma)^{10,11}B$ reactions have an advantage for α-particle studies as they have quite narrow resonances in a broad range of energies, from 0.4 MeV to 4 MeV [98]. The rate of the resonant related γ-rays is proportional to the number of confined α-particles within the resonance energy, and several resonances are required to build up the α-particle energy distribution. The main drawback of these reactions is rather low cross-sections (in the μb-range). Hence, applications of these reactions are restricted by experiments with a low neutron-induced background, for example, it could be *T–T* or *D–*^{3}*He* plasmas. Increasing the α-particle production in *D–*^{3}*He* plasmas could be done by *D*-NBI heating of the deuterium plasma with as high as possible ^{3}*He*-concentration and deuteron energies near the reaction resonance at ≈0.45 MeV.

If neon is injected as an extrinsic radiator in the plasma, the neon reactions can be utilised for α-particle studies. The energetic α-particles can generate gammas in the inelastic scattering reactions $^{20,22}Ne(\alpha,\alpha'\gamma)^{20,22}Ne$. To overcome the Coulomb repulsion and to excite the nucleus, α-particles should tunnel through the barrier, which is rather high, i.e. $U_C \approx 5.5$ MeV. Figure 31 shows that the inelastic scattering of

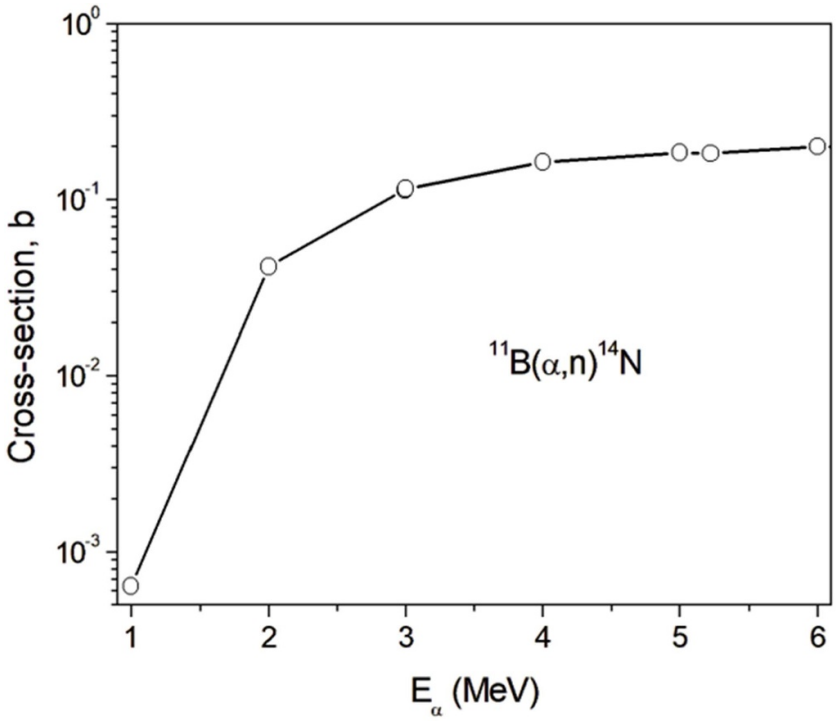

Figure 30. Evaluated total nuclear reaction cross-section of $^{11}B(\alpha,n)^{14}N$ [58].

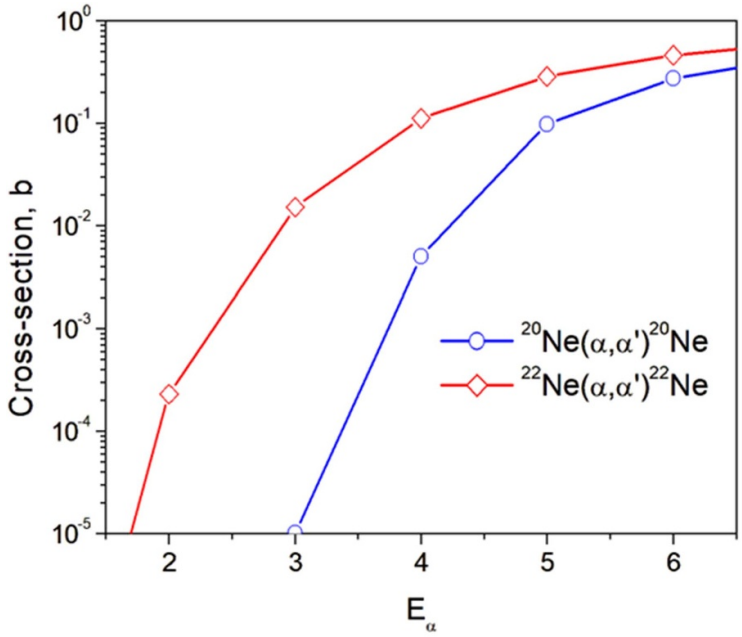

Figure 31. Evaluated total nuclear reaction cross-sections of $^{20,22}Ne(\alpha,\alpha')^{20,22}Ne$ [58].

α-particles on ^{22}Ne has a much higher cross-section than in the case of ^{20}Ne, i.e. for 3.5 MeV α-particles it is ≈65 mb in comparison to ≈2.5 mb. Though ^{22}Ne isotope abundance is ≈9%, the $^{22}Ne(\alpha,\alpha'\gamma)^{22}Ne$ reaction could provide a higher γ-ray emission rate than the $^{20}Ne(\alpha,\alpha'\gamma)^{20}Ne$ reaction. The γ-ray transition 2^+-0^+ (1.275 MeV) is strongest in ^{22}Ne but extra energetic alphas could also excite 4^+ and 2^+ states, which decay with 2.083 MeV and 3.181 MeV γ-rays (see the ^{22}Ne level scheme in figure 32). In the case of ^{20}Ne, the strongest γ-ray transition (2^+–0^+) is 1.634 MeV.

Most of the $Ne + \alpha$ nuclear reactions are endothermic, $Q < 0$, so the reactions require an additional energy input which means there is a reaction threshold for α-particles. The only exothermic ones are radiative capture reactions $^{20,22}Ne(\alpha,\gamma)^{24,26}Mg$. These reactions could be practical for diagnostics only in low-activation plasmas because their

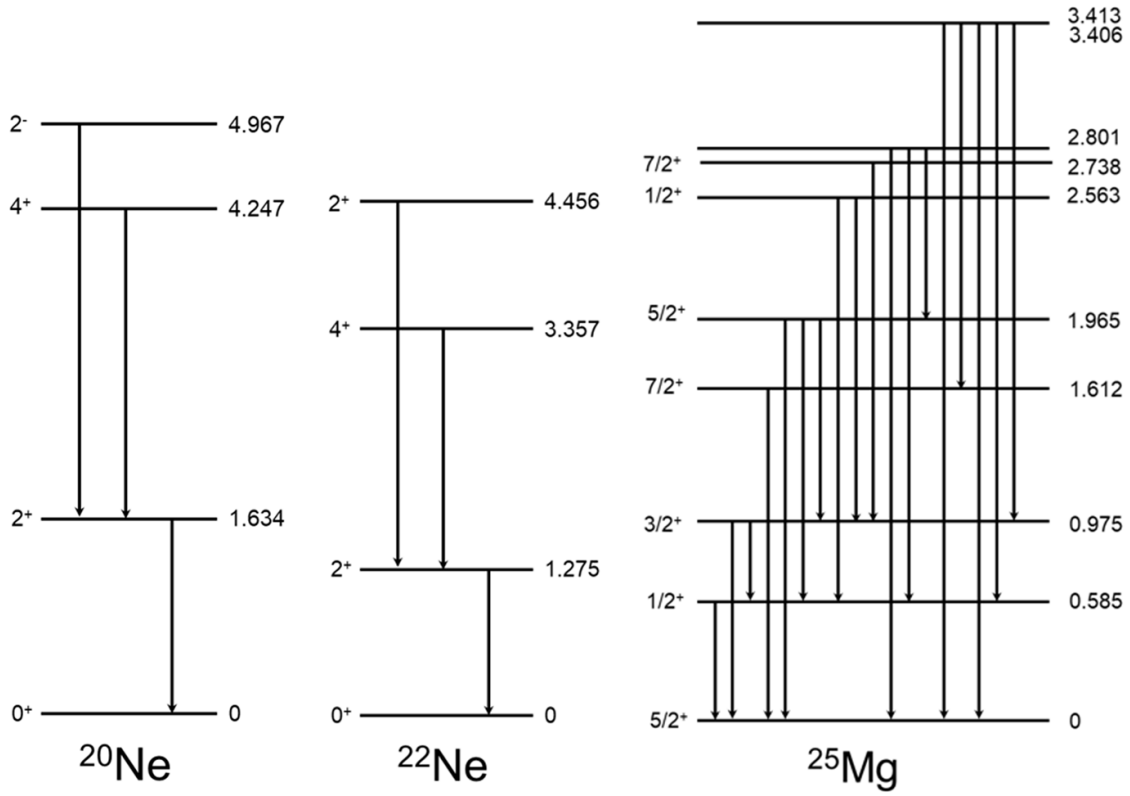

Figure 32. ^{20}Ne, ^{22}Ne and ^{25}Mg level schemes with γ-ray transitions [58].

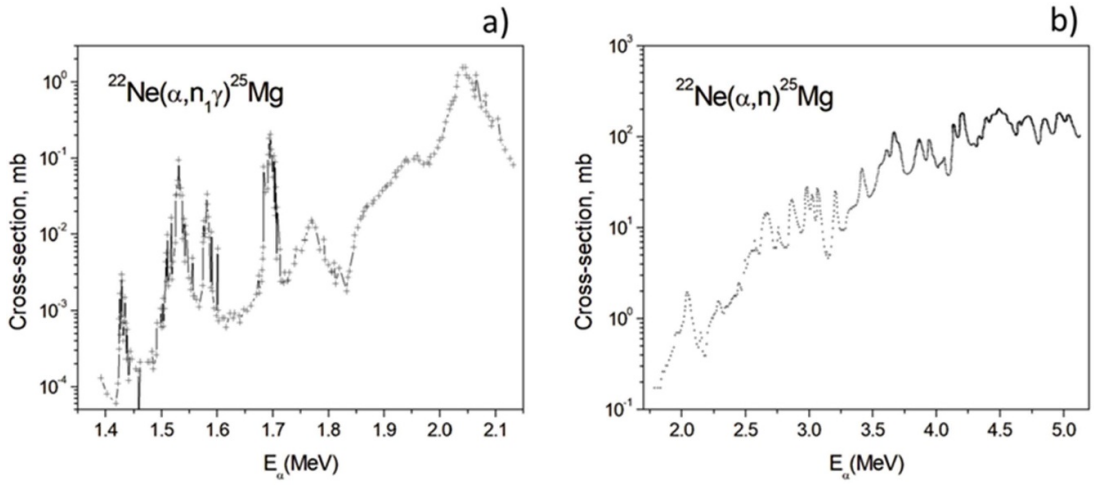

Figure 33. Experimental cross-sections. (*a*) $^{22}Ne(\alpha,n_1)^{25}Mg$ reaction (population of the first excited state of ^{25}Mg) [100]. (*b*) Total cross-section of the $^{22}Ne(\alpha,n)^{25}Mg$ reaction [101].

cross-sections are rather low [99], i.e. for alphas in the range 2.5–5.5 MeV, the cross-section of the $^{20}Ne(\alpha,\gamma)^{24}Mg$ reaction is ∼5 μb and the $^{22}Ne(\alpha,\gamma)^{26}Mg$ cross-section is even lower. Gamma-rays to the ground and first excited states have energies $E_\gamma \approx Q_{0,1} + E_{c.m}$.

The endothermic $^{22}Ne(\alpha,n\gamma)^{25}Mg$ reaction has $Q = -0.478$ MeV. There are low-lying excited states in ^{25}Mg (figure 32), so the first level can be excited by alphas with $E_\alpha > 1.4$ MeV. The measured excitation function [100] of this level is shown in figure 33(*a*). The total cross-section of the neutron production in the $^{22}Ne(\alpha,n)^{25}Mg$ reaction with α-particles in the energy range $E_\alpha > 2.3$ MeV [101] is presented in figure 33(*b*); the excited states of ^{25}Mg are discharged by γ-rays with $E_\gamma < 3.41$ MeV (see the ^{25}Mg level scheme and γ-ray transitions in figure 32).

6. Summary and conclusions

A severe fusion reactor environment is the reason that some conventional plasma diagnostics are not feasible. However, γ-ray diagnostics can be used in burning plasma reactors without direct access to the vacuum vessel, and the feasibility of γ-ray measurements for monitoring the *D–T* fusion rate and diagnosing confined α-particles was confirmed in the recent *D–T* experiments on JET. Using previous experience of the γ-ray diagnostic operation on JET, various applications of γ-ray diagnosis in present devices and future reactors were proposed in this paper. Gamma-ray measurements can provide diagnostic information in all reactor exploitation phases, both low-activation (*H/D/T/He*) and burning *D–T* plasmas, including the initial setup of plasma discharges, which is considered detection of REs during the plasma current ramp-up and in the case of disruptions. The γ-ray diagnosis of fast-ions (*H, D, T,* ^{3}*He*) can be used to optimise auxiliary plasma heating systems as well as deuterium and *D–T* plasma scenarios. Special consideration in the paper focuses on the γ-ray diagnosis of α-particles in *D–T* and low-activation plasmas, as well as the *D–T* burn monitoring, enabling the inference of temperature and *DT*-fuel ratio in the core, and which are thus key duties of the burning plasma γ-ray diagnostics. For this purpose, nuclear reactions giving rise to appropriate γ-rays for measurements in plasmas with *Li, B, C* and *Ne* impurities were selected and recommendations for usage of these reactions based on previous JET experience are provided.

During the selection of γ-ray diagnostic reactions, a lack or ambiguity of the important nuclear cross-sections was found. Seeing as wall boronisation is considered in most fusion devices, reaction cross-section measurements with boron targets, using *p-, d-,* ^{3}*He-* and ^{4}*He*-beams, are recommended. Data on the α-particle reactions, $^{10,11}B(\alpha,n\gamma)^{13,14}N$ and $^{10}B(\alpha,p\gamma)^{13}C$, are of crucial importance for α-particle confinement studies and their monitoring in future burning plasma reactors. In addition, cross-section measurements of the following reactions: $^{10,11}B(d,n\gamma)^{11,12}C$, $^{11}B(d,\alpha\gamma)^{9}Be$, $^{10}B(d,p\gamma)^{11}B$, $^{11}B(^3He,pn\gamma)^{12}C$ are required for the commissioning and characterisation of the auxiliary heating and plasma scenario development.

In conclusion, this paper provides an opportunity for designing and modelling diagnostic systems for burning plasma machines, as well as testing them in currently working fusion devices in preparation for the exploitation of the forthcoming SPARC and ITER.

Acknowledgments

The authors wish to thank Dr K.G. McClements (UKAEA) and Dr D.L. Keeling (UKAEA) for useful discussions. This work has been carried out within the framework of the EUROfusion Consortium, funded by the European Union via the Euratom Research and Training Programme (Grant Agreement No. 101052200—EUROfusion) and from the EPSRC (Grant Numbers EP/W006839/1). To obtain further information on the data and models underlying this paper please contact PublicationsManager@ukaea.uk. Views and opinions expressed are, however, those of the author(s) only and do not necessarily reflect those of the European Union or the European Commission. Neither the European Union nor the European Commission can be held responsible for them.

ORCID iDs

V.G. Kiptily 0000-0002-6191-7280
Ye.O. Kazakov 0000-0001-6316-5441

References

[1] Salewski M. *et al* 2025 *Nucl. Fusion* **65** 043002
[2] Maggi C.F. *et al* 2024 *Nucl. Fusion* **64** 112012
[3] ITER Physics Basis Editors, ITER Physics Expert Group Chairs and Co-Chairs and ITER Joint Central Team and Physics Integration Unit 1999 *Nucl. Fusion* **39** 2137
[4] Fasoli A. *et al* ITER Physics Basis 2007 *Nucl. Fusion* **47** S264
[5] Creely M. *et al* 2020 *J. Plasma Phys.* **86** 865860502
[6] Harman J. 2012 DEMO operational concept description Report No. 2LCY7A, EUROfusion/EFDA
[7] Meyer H. 2024 *Phil. Trans. R. Soc. A* **382** 20230406
[8] Kiptily V.G., Cecil F.E. and Medley S.S. 2006 *Plasma Phys. Control. Fusion* **48** R59
[9] Kiptily V.G. *et al* 2002 *Nucl. Fusion* **42** 999
[10] Iliasova M. *et al* 2022 *Nucl. Inst. Methods Phys. Res. A* **1031** 166586
[11] Kiptily V.G. *et al* 2023 *Phys. Rev. Lett.* **131** 075101
[12] Kiptily V.G. *et al* 2024 *Nucl. Fusion* **64** 086059
[13] Mantsinen M.J. *et al* 2002 *Phys. Rev. Lett.* **88** 15002
[14] Mantsinen M.J. *et al* 2002 *Phys. Rev. Lett.* **89** 15004
[15] Mayoral M.-L. *et al* 2006 *Nucl. Fusion* **46** S550
[16] Kiptily V.G. *et al* 2012 *Plasma Phys. Control. Fusion* **54** 074010
[17] Kiptily V.G. *et al* 2010 *Nucl. Fusion* **50** 084001
[18] Nocente M. *et al* 2012 *Nucl. Fusion* **52** 063009
[19] Tardocchi M. *et al* 2011 *Phys. Rev. Lett.* **107** 205002
[20] Kiptily V.G. *et al* 2022 *Plasma Phys. Control. Fusion* **64** 064001
[21] Nocente M. *et al* 2010 *Rev. Sci. Instrum.* **81** 10D321
[22] Curuia M. *et al* 2017 *Fusion Eng. Des.* **123** 749
[23] Nocente M. *et al* 2021 *Rev. Sci. Instrum.* **92** 043537
[24] Adams J.M., Jarvis O.N., Sadler G.J., Syme D.B. and Watkins N. 1993 *Nucl. Inst. Methods Phys. Res. A* **329** 277
[25] Jarvis O.N. 1997 *Plasma Phys. Control. Fusion* **39** 1571
[26] Kiptily V.G. *et al* 2005 *Nucl. Fusion* **45** L21
[27] Kiptily V.G. *et al* 2009 *Nucl. Fusion* **49** 065030
[28] Kiptily V.G. *et al* 2013 *Plasma Fusion Res.* **8** 2502071
[29] Kazakov Y.O. *et al* 2017 *Nat. Phys.* **13** 973
[30] Kiptily V.G. *et al* 1990 *Fusion Technol.* **18** 583
[31] Kiptily V.G., Matjukov A.V., Mishin A.S., Najdenov V.O., Polunovskij I.A., Rassadin L.A. and Chugunov I.N. 1992 *Fusion Technol.* **22** 454
[32] Kiptily V.G., Baranov Y.F., Barnsley R., Bertalot L., Hawkes N.C., Murari A., Popovichev S., Sharapov S.E., Stork D. and Yavorskij V. 2004 *Phys. Rev. Lett.* **93** 115001
[33] Chugunov I.N., Shevelev A.E., Gin D.B., Kiptily V.G., Gorini G., Nocente M., Tardocchi M., Doinikov D.N., Naidenov V.O. and Khilkevitch E.M. 2011 *Nucl. Fusion* **51** 083010
[34] Barabaschi P., Fossen A., Loarte A., Becoulet A. and Coblentz L. 2025 *Fusion Eng. Des.* **215** 114990
[35] Loarte A. *et al* 2025 *Plasma Phys. Control. Fusion* **67** 065023

[36] Campbell D.J. *et al* 2024 *ITER research plan within the staged approach (level III—final version)* ITER Technical Report, ITR-24-005
[37] Winter J. 1996 *Plasma Phys. Control. Fusion* **38** 1503
[38] Bodner G. *et al* 2022 *Nucl. Fusion* **62** 086020
[39] Kaita R. 2019 *Plasma Phys. Control. Fusion* **61** 113001
[40] Princeton Plasma Physics Laboratory *Tokamak Fusion Test Reactor (TFTR)* (available at: https://www.pppl.gov/tokamak-fusion-test-reactor)
[41] Snipes J.A. *et al* 1992 *J. Nucl. Mater.* **196–198** 686
[42] De Vries P.C., Gribov Y., Martin-Solis R., Mineev A.B., Sinha J., Sips A.C.C., Kiptily V. and Loarte A. 2020 *Plasma Phys. Control. Fusion* **62** 125014
[43] De Vries P.C. *et al* 2023 *Nucl. Fusion* **63** 086016
[44] Esposito B., Martín-Solís J.R., Poli F.M., Mier J.A., Sánchez R. and Panaccione L. 2003 *Phys. Plasmas* **10** 2350
[45] Shevelev A.E., Khilkevitch E.M., Kiptily V.G., Chugunov I.N., Gin D.B., Doinikov D.N., Naidenov V.O., Litvinov A.E. and Polunovskii I.A. 2013 *Nucl. Fusion* **53** 123004
[46] Shevelev A.E. *et al* 2014 *AIP Conf. Proc.* **1612** 125
[47] Khilkevitch E.M., Shevelev A.E., Chugunov I.N., Naidenov V.O., Gin D.B. and Doinikov D.N. 2013 *Tech. Phys. Lett.* **39** 63
[48] Khilkevitch E.M., Shevelev A.E., Chugunov I.N., Iliasova M.V., Doinikov D.N., Gin D.B., Naidenov V.O. and Polunovsky I.A. 2020 *Nucl. Inst. Methods Phys. Res. A* **977** 164309
[49] Ćirić D. *et al* 2011 *Fusion Eng. Des.* **86** 509
[50] King D.B. *et al* 2023 *Nucl. Fusion* **63** 112005
[51] Van Zeeland M.A. *et al* 2024 *Nucl. Fusion* **64** 056033
[52] Van Eester D. *et al* 2012 *Plasma Phys. Control. Fusion* **54** 074009
[53] Bosch H.-S. and Hale G.M. 1992 *Nucl. Fusion* **32** 611
[54] Cecil F.E., Cole D.M., Philbin R., Jarmie N. and Brown R. 1985 *Phys. Rev. C* **32** 690
[55] Buss W., Del Bianco W., Waffler H. and Zeigler B. 1968 *Nucl. Phys. A* **112** 47
[56] King H.T., Meyerhof W.E. and Hirko R.G. 1972 *Nucl. Phys. A* **178** 337
[57] Terwagne G. 1997 *Nucl. Inst. Methods Phys. Res. B* **122** 1
[58] IAEA IAEA Nuclear Data (available at: www-nds.iaea.org)
[59] Ajzenberg-Selove F. 1979 *Nucl. Phys. A* **320** 1
[60] Ajzenberg-Selove F. 1988 *Nucl. Phys. A* **490** 1
[61] Blatt S.L., Young A.M., Ling S.C., Moon K.J. and Porterfield C.D. 1968 *Phys. Rev.* **176** 1147
[62] Newman D.E. and Cecil F.E. 1984 *Nucl. Inst. Methods Phys. Res. A* **227** 339
[63] Tišma I., Lipoglavšek M., Mihovilovič M., Markelj S., Vencelj M. and Vesić J. 2019 *Eur. Phys. J. A* **55** 137
[64] Mazumdar I. 2020 *J. Astrophys. Astron.* **41** 32
[65] Marcucci L.E., Mangano G., Kievsky A. and Viviani M. 2016 *Phys. Rev. Lett.* **116** 102501
[66] Griffiths G.M., Larson E.A. and Robertson L.P. 1962 *Can. J. Phys.* **40** 402
[67] Rolfs C. and Trautvetter H.P. 1978 *Annu. Rev. Nucl. Part. Sci.* **28** 115
[68] Canon R.S. *et al* 2002 *Phys. Rev. C* **65** 044009
[69] Hahn K.I., Brune C.R. and Kavanagh R.W. 1995 *Phys. Rev. C* **51** 1624
[70] Kiptily V.G., Chugunov I.N., Naidenov V.O., Polunovski I.A. and Shevelev A.E. 1999 *Plasma Dev. Oper.* **7** 255
[71] Sikora M.H. and Weller H.R. 2016 *J. Fusion Energy* **35** 538
[72] He J.J. *et al* 2016 *Phys. Rev. C* **93** 055804
[73] Segel R.E., Hanna S.S. and Allas R.G. 1965 *Phys. Rev.* **139** B818
[74] Burtebaev N. *et al* 2008 *Phys. Rev. C* **78** 035802
[75] Gyürky G., Csedreki L., Szücs T., Kiss G.G., Halász Z. and Fülöp Z. 2023 *Eur. Phys. J. A* **59** 59
[76] Schneider P. *et al* 2023 *Nucl. Fusion* **63** 112010
[77] Parporttas Y. *et al* 2006 *Phys. Rev. C* **74** 015804
[78] Yan J. *et al* 1997 *Phys. Rev. C* **55** 1890
[79] Papillon F. and Walter P. 1997 *Nucl. Inst. Methods Phys. Res. B* **132** 468
[80] Källne J., Batistoni P., Gorini G., Huxtable G.B., Pillon M., Podda S. and Rapisarda M. 1988 *Nucl. Fusion* **28** 1291
[81] Conroy S., Jarvis O.N., Sadler G. and Huxtable G.B. 1988 *Nucl. Fusion* **28** 2127
[82] Strachan J.D., McCauley J.S., Munsat T., Barnes C.W., Budny R.V., Jassby D.L., Johnson L.C., McCune D.C. and Roquemore A.L. 1996 *Nucl. Fusion* **36** 1189
[83] Nishitani T., Hoek M., Harano H., Isobe M., Tobita K., Kusama Y., Wurden G.A. and Chrien R.E. 1996 *Plasma Phys. Control. Fusion* **38** 355
[84] Ballabio L., Frenje J., Källne J., Conroy S.W., Ericsson G., Tardocchi M., Traneus E. and Gorini G. 2000 *Nucl. Fusion* **40** 21
[85] Kiptily V.G., Belli F., Eriksson J., Hellesen C., Goloborodko V. and Schoepf K. 2019 *Nucl. Fusion* **59** 064001
[86] Kiptily V.G. *et al* 2015 *Nucl. Fusion* **55** 023008
[87] Allen K.W., Almqvist E., Dewan J.T., Pepper T.P. and Sanders J.H. 1951 *Phys. Rev.* **82** 262
[88] Kiptily V.G. *et al* 1996 ITER gamma diagnostics: 2-D neutron and gamma camera *Diagnostics for Experimental Thermonuclear Fusion Reactors* ed P.E. Stott, G. Gorini and E. Sindoni (Plenum Press)
[89] Kiptily V.G. 2025 *Fusion Eng. Des.* **215** 114959
[90] Liu Q. *et al* 2020 *Phys. Rev. C* **101** 025808
[91] Kiptily V.G. *et al* 2018 *Nucl. Fusion* **58** 082009
[92] Gassner T., Schoepf K., Sharapov S.E., Kiptily V.G., Pinches S.D., Hellesen C. and Eriksson J. 2012 *Phys. Plasmas* **19** 032115
[93] Kazakov Y.O. *et al* 2021 *Phys. Plasmas* **28** 020501
[94] Coelho R. *et al* Alpha particle generation and confinement in D-3He scenarios in JT-60SA IAEA Conference pre-print, IAEA-FEC2025
[95] Kazakov Y.O. *et al* Insights from fast-ion physics studies on JET in support of JT-60SA and ITER rebaseline IAEA Conference pre-print, IAEA-FEC2025
[96] Ogawa K., Magee R.M., Tajima T., Gota H., McCarroll P., Allfrey I., Nuga H., Isobe M. and Osakabe M. 2024 *Nucl. Fusion* **64** 096028
[97] Kamio S. *et al* 2026 *Nucl. Fusion* **66** 036020
[98] Cecil F.E., Zweben S.J. and Medley S.S. 1986 *Nucl. Inst. Methods Phys. Res. A* **245** 547
[99] Kuhlmann E. *et al* 1975 *Phys. Rev. C* **11** 1525
[100] Harms V., Kratz K.-L. and Wiescher M. 1991 *Phys. Rev. C* **43** 2849
[101] Haas F.X. and Bair J.K. 1973 *Phys. Rev. C* **7** 2432